The influence of gas pore pressure in dense granular flows: numerical simulations versus experiments and implications for pyroclastic density currents

Alvaro Aravena, Laurent Chupin, Thierry Dubois, Olivier Roche

The influence of gas pore pressure in dense granular flows: numerical simulations versus experiments and implications for pyroclastic density currents

Alvaro Aravena[1,2], Laurent Chupin[2], Thierry Dubois[2], Olivier Roche[1]

[1]Laboratoire Magmas et Volcans, Université Clermont Auvergne, CNRS, IRD, OPGC, Clermont-Ferrand, France.

[2]Laboratoire de Mathématiques Blaise Pascal, Université Clermont Auvergne, CNRS, Clermont-Ferrand, France.

Corresponding author: Alvaro Aravena (alvaro.aravena@uca.fr).

Abstract

We investigate the influence of gas pore pressure in granular flows through numerical simulations on horizontal and low-angle inclined surfaces. We present a two-phase formulation that allows description of dam-break experiments considering high-aspect-ratio collapsing columns and depth-dependent variations of flow properties. The model is confirmed by comparing its results with data of analogue experiments. The results suggest that a constant, effective pore pressure diffusion coefficient can be determined in order to reproduce reasonably well the dynamics of the studied dam-break experiments, with values of the diffusion coefficient consistent with experimental estimates from defluidizing static columns. The discrepancies between simulations performed using different effective pore pressure diffusion coefficients are mainly observed during the early acceleration stage, while the final deceleration rate, once pore pressure has been dissipated, is similar in all the studied numerical experiments. However, these short-lasting discrepancies in the acceleration stage can be manifested in large differences in the resulting run-out distance. We also analyze the pore pressure at different distances along the channel. Although our model is not able to simulate the under-pressure phase generated by the sliding head of the flows in experiments and measured beneath the flow-substrate interface, the spatio-temporal characteristics of the subsequent over-pressure phase

are compatible with experimental data. Additionally, we studied the deposition dynamics of the granular material, showing that the timescale of deposition is much smaller than that of the granular flow, while the time of the deposition onset varies as a function of the distance from the reservoir, being strongly controlled by the surface slope angle. The simulations reveal that an increment of the surface slope angle from 0° to 10° is able to increase significantly the flow run-out distance (by a factor between 2.05 and 2.25, depending on the fluidization conditions). This has major implications for pyroclastic density currents, which typically propagate at such gentle slope angles.

1. Introduction

Pyroclastic density currents (PDCs) are gravity-driven flows of hot particles (pyroclasts and lithic fragments) and gas (Druitt 1998; Branney and Kokelaar 2002; Dufek et al. 2015; Dufek 2016) generated by the partial or total collapse of an eruptive column or a volcanic dome. They exhibit a wide range of particle concentration, temperature and grain size distribution, and two physical regimes can be recognized as end-members (Branney and Kokelaar 2002; Burgisser and Bergantz 2002; Dufek 2016): dilute and dense flows, which may occur alone (e.g. dilute turbulent flow) or simultaneously (e.g. dense base and overriding turbulent part) during the propagation of a PDC. The dilute component of PDCs consists in a turbulent suspension with a solid concentration of the order of 1 vol. % or less dominated by the interaction between solid particles and the interstitial gas, while the dynamics of the dense component of PDCs, if present, is typically dominated by particle-particle interaction and by friction with the topography, presenting a solid concentration of the order of 30 – 60 vol. % (Lube et al. 2020). A transport regime of PDCs characterized by clusters at intermediate particle concentrations (i.e., a few vol.% to ~30 vol.%) has been recognized recently and may be present for instance in a transitional zone between a dense base and an upper dilute turbulent part (Breard et al. 2016;

Fullmer and Hrenya 2017; Lube et al. 2020). Because of their high propagation velocities, dynamic pressures and temperatures, PDCs can devastate urbanized zones, being one of the most hazardous processes associated with volcanic eruptions (Druitt 1998; Branney and Kokelaar 2002; Cole et al. 2015; Neri et al. 2015). Thus, deciphering the factors controlling their dynamics and the expected run-out distance is of paramount importance for volcanic hazard assessment. Although much attention has been paid to the study of the long run-out distance that characterize some PDCs (Bursik and Woods 1996; Branney and Kokelaar 2002; Kelfoun 2011; Roche et al. 2016, 2021; Shimizu et al. 2019; Giordano and Cas 2021), several aspects remain poorly understood. PDC run-out distance is the result of a series of concomitant processes whose relative efficiency is influenced by the flow properties (e.g. solid particle concentration, volume, speed and temperature) and the regional slope (Valentine et al. 2011), and include: the interaction with the surrounding atmosphere (e.g., air entrainment and heat transfer; Benage et al. 2016), the rheological effect of interstitial pore fluid pressure (Druitt et al. 2007; Roche 2012), and the interplay between the flow base and the substrate, where different processes may occur, such as erosion (Cas et al. 2011; Bernard et al. 2014; Farin et al. 2014), self-channelization (Brand et al. 2014; Gase et al. 2017), self-fluidization (Breard et al. 2018; Chédeville and Roche 2018), and pyroclast deposition (Branney and Kokelaar 2002).

In particular, within the pyroclastic mixture, and especially at the impact zone of a collapsing fountain (Sweeney and Valentine 2017; Valentine and Sweeney 2018; Valentine 2020; Fries et al. 2021), the differential motion between the interstitial gas (flowing relatively upwards) and the solid particles (moving relatively downward) is able to generate pore pressure, which counterbalances the weight of the particles, reduces friction and thus increases run-out distance (Iverson 1997; Savage and Iverson 2003; Goren et al. 2010; Roche 2012; Rowley et al. 2014; Breard et al. 2019a). The temporal evolution of pore pressure, and thus its effective influence on run-out distance, depends on the balance between some source mechanisms (e.g. gas ingestion, differential gas-particle motion caused by particle settling) and pore pressure diffusion, which is in turn controlled by the properties of the PDC material. In fact, slow gas pressure diffusion is favored by thick pyroclastic flows and by grain size distributions dominated by fine particles that confer low hydraulic permeability (Druitt et al. 2007; Burgisser 2012; Roche 2012; Breard et al. 2019b).

In this work we address the influence of pore pressure on the propagation of granular flows through numerical simulations. In particular, we present a two-phase model, built on the formulation presented by Chupin et al. (2021), which accounts for the effect of pore pressure on the dynamics of granular flows and allows us to simulate collapsing columns in the dam-break configuration and the subsequent flow propagation on horizontal and low-angle inclined surfaces. The column height and aspect ratio adopted in our numerical simulations (40 cm and 2, respectively) were selected to allow model confirmation by comparing numerical results with published experimental data (cf. Valentine 2019; Esposti Ongaro et al. 2020) of collapsing columns over a horizontal surface (Roche et al. 2010). Note that we use the term *confirmation* instead of *validation* following the framework presented by Esposti Ongaro et al. (2020). Numerical results also allow us to explore some key physical aspects controlling the dynamics of granular flows (e.g. pore pressure spatio-temporal evolution and flow deposition), which are often difficult to measure in time across the entire spatial domain of analogue experiments. Moreover, adopting a set of input conditions calibrated using experimental data, we performed additional simulations considering collapsing columns on low-angle inclined rigid surfaces, in order to test the coupled effect of pore pressure and topography on the propagation of granular flows. Compared to previous efforts to address numerically the influence of pore pressure in the propagation dynamics of PDCs (Gueugneau et al. 2017), which are based on depth averaged models, our model has some relevant strengths: it allows us to study high-aspect ratio collapsing columns and to describe depth-dependent variations of the flow properties.

This article consists of five sections. In Section 2 we describe the experimental configuration considered in this paper. In Section 3, we present the numerical model adopted (Section 3.1), its confirmation by comparing numerical results with those of analogue experiments (Section 3.2), and then we describe the results of simulations performed considering low-angle inclined surfaces (Section 3.3). Finally, in Sections 4 and 5 we present the discussion and concluding remarks of this article.

2. Experimental configuration

In order to test and confirm our model, we considered the experimental data presented by Roche et al. (2010). The benchmark experiment consists in the release of a fluidized granular column into a horizontal, smooth channel (note that the term *fluidization* is used here to refer to the presence of a vertical flow of air able to counterbalance the bed weight, and it is not related to the presence of other fluid phases such as water). The dynamics of the dam-break experiment, which was measured using high-speed cameras and pressure sensors located at different positions along the horizontal channel, can be decomposed into three stages: (1) a quick phase of initial acceleration, (2) propagation of the front at nearly constant velocity, and (3) deceleration of the flow and front stopping. Roche et al. (2010) and Chupin et al. (2021) also pointed out a final stage of very slow propagation of granular material in the flow body after the front stopped. The experimental apparatus includes a reservoir of 20 cm length and 10 cm width, and a channel of 3 m length and 10 cm width. Initially, the particles are introduced into the reservoir (column height of 40 cm) where an air flow is supplied from below in order to generate fluidization and the related pore pressure. This simple configuration aims to mimic particle-gas differential motion generated through various means, including particle settling (Chédeville and Roche 2018; Breard et al. 2018; Valentine and Sweeney 2018; Fries et al. 2021). Roche et al. (2010) tested two fluidization conditions by adjusting the supplied air velocity: (1) imposing the minimum fluidization velocity (U_{mf}) or (2) imposing the minimum bubbling velocity (U_{mb}). The minimum fluidization velocity U_{mf} ($\sim 0.8\ \mathrm{cm/s}$ in the experiments; Roche et al. 2010) guaranties that the bed weight is counterbalanced by the drag of the interstitial air flow on the particles, and the granular bed is not expanded. On the other hand, at U_{mb} ($\sim 1.3\ \mathrm{cm/s}$ in the experiments; Roche et al. 2010), the bed weight is counterbalanced and the granular network is expanded. In order to trigger column collapse, at $t = 0$, a sluice gate is opened rapidly ($< \sim 0.1$ s), allowing to release the granular material, which propagates laterally along the horizontal channel during about 1.3 s. As our numerical model treats incompressible flows, we compare our results with the analogue experiment performed using the minimum fluidization velocity (U_{mf}), that is, when the bed is not expanded. The particles used in these experiments were spherical glass beads with a grain size range of 60-90 μm (monodisperse size distribution, mean of 75 μm) and a density of $\rho_s = 2500\ \mathrm{kg/m^3}$. Note that more complex particle shapes and size distributions are able to control pore pressure diffusion in granular flows by affecting porosity and mixture permeability (Wilson 1984; Burgisser 2012; Breard et al. 2019b and references therein), and that Breard et al. (2019b) showed that the effective particle size regarding fluidization and pore pressure diffusion is the Sauter diameter, which is very close to the mean diameter for subspherical particles such as we considered. The resulting granular column had a bulk density of $\rho_b = 1450 \pm 50\ \mathrm{kg/m^3}$ (i.e. pore volume fraction of $\varepsilon = 0.42 \pm 0.02$). Additionally, we can calculate the theoretical hydraulic diffusion coefficient $\kappa_T = k/(\varepsilon\mu\beta)$, where k is hydraulic permeability, μ is gas dynamic viscosity and β is gas compressibility. In case of a perfect gas, $\beta = 1/P_i$, where P_i is the initial pore pressure, which is about equal to the atmospheric pressure. Considering that $k \sim 10^{-11}\ \mathrm{m^2}$, $\varepsilon \sim 0.42$, and $\mu \sim 1.8 \times 10^{-5}\ \mathrm{Pa\ s}$, we obtain $\kappa_T \sim 0.13\ \mathrm{m^2/s}$. However, it is worth noting that this value is one order of magnitude larger than the estimates of diffusion coefficient given by Roche et al. (2010) ($\kappa \sim 0.01\ \mathrm{m^2/s}$), which are based on experimental measurements on static defluidizing beds and are shown to increase with the bed height. The reason explaining this discrepancy is unknown and is discussed below.

3. Numerical simulations

3.1 Mathematical modelling and numerical schemes

Based on the numerical model presented by Chupin et al. (2021), we constructed a new model able to consider the effect of pore pressure and reproduce the experimental configuration adopted by Roche et al. (2010). We consider the collapse of a granular mass over a planar rigid surface with inclination angle θ varying from horizontal up to 10°. As the laboratory experiments have been performed in a narrow channel (10 cm wide and 3 m long; Roche et al. 2010), we consider the problem as mainly two-dimensional. Note that we neglect the effects of the lateral walls.

The granular medium, which is a mixture of air and glass beads, is described by an incompressible flow with a μ(I)-rheology (Jop et al. 2006). In this rheological model, which has been widely adopted to describe dense granular flows (Gray and Edwards 2014; Ionescu et al. 2015), the dynamics of the granular flow is governed by the mass and momentum conservation laws

$$\rho(\partial_t \boldsymbol{u} + \boldsymbol{u} \cdot \boldsymbol{\nabla} \boldsymbol{u}) = \operatorname{div} \boldsymbol{T} + \rho \boldsymbol{g}, \quad (1)$$

$$\operatorname{div} \boldsymbol{u} = 0, \quad (2)$$

$$\partial_t \rho + \boldsymbol{u} \cdot \boldsymbol{\nabla} \rho = 0, \quad (3)$$

where $\boldsymbol{u}$ is the material velocity, $\boldsymbol{g}$ is an external force (gravity), $\boldsymbol{T}$ is the total stress tensor, and $\rho = \phi \rho_s$ is the bulk density, where ρ_s and ϕ are the particle density and average volume fraction, respectively. In our simulations, based on the experimental data described by Roche et al. (2010), we use $\rho_s = 2500$ kg/m^3 and $\phi = 1 - \varepsilon = 0.58$. The pressure is given by $p =$

$-\frac{1}{3}\mathrm{tr}\,\boldsymbol{T}$, so that the deviatoric stress $\boldsymbol{T}'$ ($\boldsymbol{T} = -p\boldsymbol{Id} + \boldsymbol{T}'$) has to be prescribed in order to close equations (1) – (3).

Modeling the granular flow with equations (1) – (3) entails that the total pressure p is the sum of the solid (effective) pressure p_s, due to force chains of glass beads, and the pore pressure p_f, due to the presence of air between particles. Therefore, in order to account for the presence of air between glass beads, the pore pressure and its effect on granular flows should be modeled. Following Iverson and Denlinger (2001), the pore pressure diffuses and is advected with the granular mass so that p_f satisfies the balance equation

$$\partial_t p_f - \mathrm{div}(\kappa \boldsymbol{\nabla} p_f) + \boldsymbol{u} \cdot \boldsymbol{\nabla} p_f = 0, \qquad (4)$$

where κ is the diffusion coefficient. The knowledge of p_f through equation (4) permits us to define the effective pressure as $p_s = p - p_f$.

In the μ(I)-rheology (Jop et al. 2006), the deviatoric stress $\boldsymbol{T}'$ is given by

$$\boldsymbol{T}' = \mu(I) p_s \frac{\boldsymbol{D}(\boldsymbol{u})}{|\boldsymbol{D}(\boldsymbol{u})|}, \qquad (5)$$

where $\boldsymbol{D}(\boldsymbol{u}) = \frac{1}{2}(\boldsymbol{\nabla u} + \boldsymbol{\nabla u}^t)$ is the strain rate tensor and $|\boldsymbol{D}(\boldsymbol{u})|^2 = \frac{1}{2}\sum_{i,j} \boldsymbol{D}(\boldsymbol{u})_{i,j}^2$. The friction coefficient $\mu(I)$ depends on the inertial number I, namely

$$\mu(I) = \mu_s + \frac{\mu_\infty - \mu_s}{1 + I_0/I} \text{ and } I = \frac{2d|\boldsymbol{D}(\boldsymbol{u})|}{\sqrt{p_s/\rho_s}}. \qquad (6)$$

In equation (6), d is the particle diameter, I_0 is a dimensionless number, $\mu_s = \tan(\alpha)$ with α representing the static internal friction angle of the granular material, and $\mu_\infty \geq \tan(\alpha)$ is an asymptotic value of the friction coefficient for large inertial numbers. By combining equation (6) and equation (5) (see Chupin et al. (2021) for the details), we can rewrite the expression of the tensor $\boldsymbol{T}'$ in regions where $\boldsymbol{D}(\boldsymbol{u}) \neq 0$ as

$$\boldsymbol{T}' = 2\eta(|\boldsymbol{D}(\boldsymbol{u})|, p_s)\boldsymbol{D}(\boldsymbol{u}) + \tan(\alpha)\, p_s \frac{\boldsymbol{D}(\boldsymbol{u})}{|\boldsymbol{D}(\boldsymbol{u})|}, \qquad (7)$$

with

$$\eta(|\boldsymbol{D}(\boldsymbol{u})|, p_s) = \frac{(\mu_\infty - \tan(\alpha))p_s}{2|\boldsymbol{D}(\boldsymbol{u})| + \frac{I_0}{d}\sqrt{p_s/\rho_s}}. \quad (8)$$

With this formulation, the μ(I)-rheology appears to be a viscoplastic rheology with a Drucker-Prager plasticity criterion (see also Jop et al. 2006 and Ionescu et al. 2015) and a spatio-temporal variable viscosity, which is a fundamental aspect of our study. In order to treat the non-differentiable definition of the tensor $\boldsymbol{T}'$, due to the presence of the $1/|\boldsymbol{D}(\boldsymbol{u})|$ term that is singular in the absence of strain rate, a projection scheme is applied (Chalayer et al. 2018; Chupin et al. 2021). The projection procedure avoids a need to resort to any regularization technique and allows to accurately capture the rigid zones, i.e., the regions where no deformation occurs.

As in Chupin et al. (2021), the presence of the ambient gas (i.e. the air outside the flow) is taken into account. The granular flow and the ambient air flow are separated by an interface transported by the velocity field. A level-set function Φ (see Osher and Fedkiw (2001) for instance), initially defined as the signed distance to the interface, is used to describe the limit between the granular flow and the ambient gas. The computational domain is split so that $\Phi < 0$ corresponds to the granular flow, $\Phi > 0$ the ambient gas and $\Phi = 0$ the interface. The level-set function satisfies the equation

$$\partial_t \Phi + \boldsymbol{u} \cdot \boldsymbol{\nabla} \Phi = 0. \quad (9)$$

The ambient flow ($\Phi > 0$) is also governed by equations (1) – (3) but with a Newtonian rheology, namely $\boldsymbol{T}' = 2\eta_{\mathrm{f}}\boldsymbol{D}(\boldsymbol{u})$ where η_{f} is the air dynamic viscosity, and a mass density $\rho = \rho_{\mathrm{f}}$. Note that the pore pressure equation (4) has a meaning only inside the granular flow, that is where $\Phi < 0$. In order to solve an equation valid over the whole computational domain, the diffusion coefficient κ takes a very large value ($\approx 10^{16}\ \mathrm{m}^2/\mathrm{s}$) outside the granular flow so that p_f is extended to zero outside of the granular flow.

Coulomb friction boundary conditions are applied on the vertical backwall of the reservoir and on the bottom of the channel on which the granular medium slides, that is

$$u_n = 0 \text{ and } \boldsymbol{T}_t = -\eta_{\mathrm{b}} \boldsymbol{u}_t - \tan(\alpha_b)\,(-T_n)^+ \frac{\boldsymbol{u}_t}{|\boldsymbol{u}_t|}, \tag{10}$$

where $u_n = \boldsymbol{u} \cdot \boldsymbol{n}$ ($\boldsymbol{n}$ being the unit outward normal vector to the domain boundary) is the normal velocity and $\boldsymbol{u}_t = \boldsymbol{u} - u_n \boldsymbol{n}$ the tangential one. Similarly, for the stress we have $T_n = (\boldsymbol{T} \cdot \boldsymbol{n}) \cdot \boldsymbol{n}$ and $\boldsymbol{T}_t = \boldsymbol{T} \cdot \boldsymbol{n} - T_n \boldsymbol{n}$. In all simulations reported in this paper, the friction angle on the vertical backwall of the reservoir and on the bottom of the channel (α_b) was set to 15° (Chupin et al. 2021).

At time $t = 0$, the pore pressure p_f is initialized in the reservoir as 90% of the weight of the particles, that is, $p_f(x, y) = 0.9\rho g(H - y)$ (H being the height of the initial column), which agrees with experimental measurements (Montserrat et al. 2012). Equation (4) is supplemented with Neumann boundary conditions. On the bottom of the channel inside the reservoir, that is for $x \in [-20 \text{ cm}, 0 \text{ cm}]$ and $y = 0$, the constant air flux imposed in the experiment is modeled with a constant pressure gradient $\frac{\partial p_f}{\partial n} = -0.9\rho g$. Everywhere else on the domain boundary, a homogeneous Neumann boundary condition $\frac{\partial p_f}{\partial n} = 0$ is applied.

Equations (1) – (3) and (4) are discretized in space with second order finite volume schemes on a staggered grid. A bi-projection scheme (Chalayer et al. 2018) is applied for the temporal discretization. The level-set transport equation (9) is solved with a RK3 (third-order Runge-Kutta) TVD (total variation diminishing) scheme coupled with a fifth-order WENO (weighted essentially non-oscillatory) scheme. We also apply a reinitializing algorithm in order to maintain the level-set function to the signed-distance function to the interface between the granular and the ambient flows. Details on the numerical schemes are provided in Chupin and Dubois (2016), Chalayer et al. (2018), and Chupin et al. (2021). In order to remedy to a lack of resolution of the small scale structures outside the granular flow, due to the small value of the air viscosity, a subgrid scale (Smagorinsky) model is used (Smagorinsky 1963). This results in enhancing the viscosity of air η_{f} by adding a local eddy viscosity defined as $(C_s h)^2|\boldsymbol{D}(\boldsymbol{u})|$, where h is the mesh size and $C_s \in [0.1, 0.2]$ is the Smagorinsky constant. We used hereafter the value 0.1 for C_s in all simulations.

The code, written in F90, is parallel: the PETSc library (Balay et al. 2018a, 2018b) is used to solve the linear systems and to manage data on structured grids while communications between processes are explicitly written with MPI subroutines.

3.2 Simulations on horizontal planes

As a first step, we performed a set of simulations on horizontal surfaces using the model described in Section 3.1 and considering different values of the pore pressure diffusion coefficient (κ). Here we focus on the results of simulations that agree reasonably well with the experimental results presented by Roche et al. (2010) in terms of run-out distance, temporal evolution of the front position and profile of the flow surface, that is, with pore pressure diffusion coefficients ranging from 0.015 to 0.035 m^2/s. Interestingly, these values agree with those determined experimentally by measuring the timescale of pore pressure diffusion in static columns of heights of ~15-35 cm. For comparison purposes, we also include the results of a test simulation performed using the theoretical hydraulic diffusion coefficient ($\kappa_T \sim 0.13\ \mathrm{m}^2/\mathrm{s}$). Note that we consider constant effective diffusion coefficients (with values of 0.015, 0.025, and 0.035 m^2/s), while the diffusion coefficient likely varies during the analogue experiment due to granular material dilation and compaction. To reproduce the initial setup of the benchmark analogue experiment, in our simulations the initial height of the collapsing column is 40 cm and the initial width is 20 cm. The height of the computational domain is 45 cm, adopting a grid with 128 cells in the vertical direction (i.e. cell size of 3.5 mm).

Our model tends to under-estimate the deposit thickness in proximal domains (from <5% up to ~25%) and to over-estimate the deposit thickness in distal domains (Figs. 1a-c and 2). Still, the general shapes of the simulated final profiles of the deposits are very similar to that of the benchmark analogue experiment, i.e. profiles dipping gently downstream and with the maximum thickness located in the channel near the reservoir. This deposit shape differs clearly from that of non-fluidized granular flows, whose maximum thickness is located at the back-wall of the reservoir while the thickness decreases monotonically with distance (Roche et al. 2010; Ionescu et al. 2015). Moreover, numerical results reproduce reasonably well the three phases of propagation described by Roche et al. (2010) (Fig. 3), and the relative duration of each phase as well as the flow duration are consistent with the benchmark experiment. The dynamics of gate opening in the analogue experiment slightly affects flow propagation during the initial acceleration phase, which may explain the differences in the initial front velocity during about 10% of the simulation duration (Figs. 3). An effective diffusion coefficient (κ) of about 0.015 m^2/s reproduces the experimental run-out distance, whereas a larger values of diffusion coefficient reproduce better the maximum thickness of the deposit. Note that, because our simulations are not able to describe flow thicknesses lower than 3.5 mm (i.e. the cell size used in numerical simulations), we compare our results with filtered experimental data, that is, with no consideration of flow thicknesses below this threshold (see Fig. 3 and its caption). On the other hand, the use of the theoretical value of the diffusion coefficient (i.e. 0.130 m^2/s) fails completely in reproducing the propagation dynamics of the benchmark experiment, under-estimating significantly the run-out distance (<60% of the run-out distance measured in the benchmark experiment; Figs. 1d, 2 and 3).

The simulations performed using $\kappa = 0.015$ and $\kappa = 0.035\ \mathrm{m}^2/\mathrm{s}$ give rise to differences of about 15% in the maximum velocity reached by the flow front (Fig. 4). The phase of velocity increase lasts ~17-22% of the whole propagation time, while the constant-velocity stage, which is slightly longer for simulations with low diffusion coefficients, represents ~15-25% of the total propagation time. Most of the propagation time of the granular flows (about 60-70%) is associated with the phases of deceleration and front stopping. Our results of maximum velocity ($u/\sqrt{gH}{\sim}1.0-1.15$) are consistent with the results presented by Roche et al. (2010), which further confirm the validity of our model. Note that the initial phase is characterized by the same acceleration in all the simulations, and the main differences between our simulations are observed in the absolute duration of this stage (and thus in the velocity reached by the flow front, Fig. 4). Another interesting result is that the velocity decrease during the final phase occurs at a similar rate in all the simulations (deceleration of $\sim 0.23g$). This shows that the differences in the front velocity during early phases of flow propagation are the cause of the different run-out distances, while negligible differences are observed in the dynamics of the deceleration stage. This is consistent with the fact that, once the initial pore pressure is completely dissipated, granular flows have the same rheological behaviour. On the other hand, as observed by Roche (2012), during the stopping stage the run-out distance increases with time to the power of 1/3.

The evolution of the pore pressure (Fig. 5) is the result of the coupled effect of diffusion, which occurs at a rate controlled by κ, and advection, controlled by flow velocity and thus in turn influenced by κ. Basal pore pressure undergoes an initial phase dominated by advection (i.e. advance of the iso-pressure fronts, which indicate the position along the x-axis at which specific values of pore pressure are reached as a function of time; Fig. 6), and a later phase dominated by diffusion (i.e. recession of the iso-pressure fronts) until stationary conditions are reached (Fig. 6). In particular, the simulations with $\kappa = 0.025\ \mathrm{m}^2/\mathrm{s}$ and $\kappa = 0.035\ \mathrm{m}^2/\mathrm{s}$ show a smooth, gradual transition between both phases. Instead, some of the iso-pressure fronts (Fig. 6) for the simulation with $\kappa = 0.015\ \mathrm{m}^2/\mathrm{s}$ show a significantly longer phase dominated by advection and then an abrupt decrease of pore pressure near the front. This rapid pore pressure decrease is favored by the small thickness of the granular flow at the front, while in the other cases such small flow thicknesses are reached while the flow is already defluidized.

In order to further compare our results with experimental data (Roche et al. 2010), we studied the pore pressure signal at different points along the channel base. Note that the under-pressure phase measured in experiments beneath the flow-substrate interface during the passage of the sliding head of the flow cannot be computed in our numerical simulations. Still, in Figure 7a-c we show the evolution of the modeled basal pore pressure at specific points along the x-axis, and we also display the differential pressure measured in the benchmark experiment (in the channel base at $x = 0.2$ m). The experimental data show that the passage of the flow front at a given point is followed by a short under-pressure phase and a later and longer over-pressure phase. Roche et al. (2010) propose that the under-pressure stage is mainly caused by the basal slip boundary condition and possibly by dilatancy processes (Garres-Díaz et al. 2020; Bouchut et al. 2021), which is supported by simulations (Breard et al. 2019a). Moreover, the minimum value reached during the under-pressure phase was empirically correlated to the slip velocity (u_{slip}; Roche 2012). The over-pressure phase would be instead dominated by compaction and advection of pore pressure within the granular flow. Since our model does not consider changes in density, it is not able to describe the effect of dilatancy and compaction, and thus under-pressure cannot be modeled, while the over-pressure phase, which is observed in our numerical simulations, is exclusively a consequence of advection (Fig. 7a-c). The relationship between distance along the x-axis and the maximum basal pore pressure reached is remarkably consistent with experimental data both in the curve shape and in the values measured (Fig. 7d), which further confirms the validity of the description of pore pressure used in our model once the under-pressure phase is finished, suggesting that the effect of compaction is limited compared to pore pressure advection. Note that the absence of dilatancy in our model is likely manifested in an earlier peak of the basal pore pressure than that expected in presence of an initial under-pressure stage (Fig. 7e).

Roche (2012) proposed that the basal under-pressure measured at the head of granular flows scales with the square of the flow front velocity. Based on this observation, Breard et al. (2019a) showed that the differential pressure measured in experiments can be given by

$$p_c = p_f - \frac{1}{2}\rho_b\left(u_{\text{slip}}\right)^2 , \tag{11}$$

where p_f is the basal pore pressure and ρ_b is the mixture density at the base. The use of this expression and our numerical results show that the temporal evolution of p_c at different positions along the channel is characterized by a short under-pressure phase followed by a longer over-pressure stage in proximal domains ($x < 0.5$ m, Fig. 8a-c), while distal points present only the under-pressure phase (Fig. 8a-c) because most of the pore pressure is already dissipated at these distances from the reservoir. Although the duration of the under-pressure phase of p_c is shorter than that measured in the benchmark experiment, the simulated minimum values, their evolution with distance and the time at which these values are reached are strongly consistent with experimental data (Fig. 8d-e). On the other hand, while the maximum values of p_c and those of experimental data are in agreement, the times at which these maximum values are observed are shifted.

The deposition dynamics of particles in the simulations is shown in Figure 9. Note that these results are a direct consequence of the rheological model adopted and no calibrated inputs of sedimentation rate are needed to parametrize the deposition of granular material. The length of the sliding head (L_h, Fig. 9a) was computed considering that sedimentation occurs at the base of the channel when the slip velocity reaches a value lower than 5% of the maximum slip velocity observed during the simulation. On the other hand, the variable A_d (area of material deposited, Fig. 9a) was calculated by considering the modulus of velocity in each cell of the computational grid. In particular, at a given distance from the reservoir, the thickness of the deposit was computed considering all the cells with a velocity modulus lower than 0.1 m/s (i.e. about 5% of the maximum value of the velocity modulus observed during the simulations). Our simulations show maximum lengths of the flow head of the order of 0.85-1.15 m, slightly larger than the experimental estimates of Roche (2012) (i.e. ~0.7 m; Fig. 9b) and twice the values simulated and observed in analogue experiments of dry granular flows of the same dimensions (i.e. 0.4 – 0.5 m; Roche 2012; Chupin et al. 2021). The relationship between L_h/L and L_d/L_f (see Fig. 9a for definition) shows a linear trend, in agreement with experimental data and also with the behaviour of dry granular flows (Roche 2012; Chupin et al. 2021; Fig. 9c). The evolution of the deposit area compared with the normalized time and run-out distance is also consistent with experimental data. Most of the deposition occurrs during the final 40% of the propagation time-span, when the flow front has already travelled more than 80% of the final run-out distance (Fig. 9d-e). The results show that most of the deposition occurs between $t \approx 4.0\sqrt{H/g}$ and $t \approx 6.0\sqrt{H/g} - 6.5\sqrt{H/g}$ (Fig. 9f-g) and that lowering the pore pressure diffusion coefficient leads to delayed deposition. The position at which the peak of sedimentation rate occurs increases monotonically with time in all the simulations presented, showing slightly S-shaped curves that start in the vicinity of the reservoir and present maximum advance velocities similar in all the cases ($u_{sp}/\sqrt{gH} \sim 1.4$, where u_{sp} is the advance velocity of the position of the deposition rate peak), significantly higher that the flow front velocity (Fig. 9f). Thus, our results suggest that the advance of the position of maximum deposition rate is poorly correlated with the behaviour of the flow front. At a given point along the channel, the deposition of particles tends to occur very rapidly (Fig. 9g). In fact, the time elapsed between the deposition of 10% and 90% of the final deposit at a given point is of the order of $0.1\sqrt{H/g}$, one order of magnitude smaller than the granular flow duration (Fig. 9g). Locally, the sedimentation rate reaches peaks of the order of 1 m/s, with mean sedimentation rates of the order of 0.1 m/s. It is worth noting, however, that this constraint of sedimentation rate is strongly influenced by the threshold used to define the deposited portion of the granular flow during its propagation.

3.3 Simulations on inclined planes

In the previous section we showed that the effective diffusion coefficient required to simulate the benchmark analogue experiment (Roche et al. 2010), which is likely variable in time and position, is in the range $\kappa = 0.015 - 0.035\ \mathrm{m}^2/\mathrm{s}$. Considering these values of diffusion coefficient, we investigated the coupled effect of fluidization and topography through an additional set of simulations adopting variable surface slope angles (from 0° to 10°). Additionally, for comparison purposes, we did complementary dam-break simulations considering inclined surfaces and dry flows, using the model described in Chupin et al. (2021). Thereby, simulations results for run-out distance allow quantifying the combined effects of pore pressure and surface slope angle.

The temporal evolution of the front position of dry and fluidized granular flows shows that a small increment of the surface slope angle is able to significantly increase the maximum run-out distance (Fig. 10). For instance, an increment of surface slope from 0° to 10° is able to increase the modelled run-out distance from $\sim 2H$ to $\sim 4.4H$ for dry granular flows (relative increase of 220%), where H is the initial column height, while an increase from $\sim 3.8H$ to $\sim 8.4H$ was computed for fluidized flows with $\kappa = 0.025\ \mathrm{m}^2/\mathrm{s}$ (relative increase of 220%). Differences in the propagation velocity between dry and fluidized granular flows are evident from early phases of flow propagation (Figs. 10 and 11). On the other hand, as observed in the simulations described in Section 3.2 for granular flows propagating on horizontal surfaces, also on inclined planes the differences between simulations performed with different diffusion coefficients are mainly manifested in the duration of the initial phase of velocity increase (and thus manifested in the maximum front velocity reached by the flow; Fig. 11). Instead, for a given slope angle, the velocity decrease during the final phase occurs at a similar rate for all the fluidized and dry flows simulated (Fig. 11). This is because, once the pore pressure has been dissipated by diffusion, the rheology of all the simulated granular flows is that of dry flows.

The deceleration of the flow front is strongly controlled by the slope angle (Fig. 11), ranging from $\sim 0.23g$ (at 0°) to $\sim 0.11g$ (at 10°). This dependency gives rise to significant differences in the modeled run-out distance as a function of surface slope angle for both dry and fluidized flows (Fig. 12).

Run-out of simulated flows also shows important aspects of pore pressure and surface slope angle effects (Fig. 12). For the range of diffusion coefficients adopted here, fluidization of the initial source is able to increase the run-out distance between $\sim 1.55H$ ($\kappa = 0.035\ \mathrm{m}^2/s$, slope angle of 0°) and $\sim 5.15H$ ($\kappa = 0.015\ \mathrm{m}^2/s$, slope angle of 10°), corresponding to an increase range of the run-out distance between ~165% and ~225%. Interestingly, the relative increase of run-out distance when fluidized granular flows are compared with dry flows is only weakly controlled by the slope angle (Fig. 12c). On the other hand, for given fluidization conditions, we note that an increase of slope angle from 0° to 10° produces an increment of the run-out distance of about 105-125%. This relative increase in the run-out distance is significantly larger than that measured in analogue experiments by Chédeville and Roche (2015) for lower-aspect ratio collapsing columns (0.5-1.0), i.e., ~60% for an increase of slope angle from 0° to 10°. We speculate that this could be a consequence of the slower pore pressure diffusion that characterize taller collapsing columns.

The slope angle has a small influence on the maximum basal pore pressure computed at a given distance (Fig. 13). This shows that the evolution of the basal pore pressure is mainly controlled by the effective pore pressure diffusion coefficient. The length of the sliding head increases significantly when granular flows propagate on inclined surfaces (Fig. 14a-c). On the other hand, inclined topographies are able to delay the onset of deposition and reduce the sedimentation rate (Fig. 14d-f). Interestingly, the shape of the curves describing the evolution of the deposit area (Fig. 14d-f) changes when different slope angles are considered. Deposition in flows propagating on horizontal surfaces occurs at a nearly constant rate during almost all the deposition stage (Fig. 14d-f), and the position at which the maximum deposition rate occurs advances at an almost constant velocity (Fig. 14g-i). However, in simulations performed at high slope angles, the initial stage of deposition, characterized by a relatively low sedimentation rate, is accompanied by a relatively slow advance of the position at which the maximum deposition rate occurs (Fig. 14g-i), while both the sedimentation rate and the advance velocity of the position of maximum deposition increase during the final period of deposition (Fig. 14d-i).

4. Discussion

In this work we have presented a new model to describe dam-break fluidized granular flows and test the effect of low-angle inclined surfaces in the resulting propagation dynamics. This model, built on the formulation described by Chupin et al. (2021) for dry flows, was compared with a benchmark analogue experiment for which detailed information of flow propagation, pore pressure evolution and sedimentation dynamics is available in the literature (Roche et al. 2010; Roche 2012). Thereby, this work complements previous efforts to analyse analogue experiments through numerical modeling (Breard et al. 2019a). In particular, Breard et al. (2019a) tested different friction models and compared their simulations with experiments considering flow shape, kinematics and pore pressure evolution. Our model allows the description of the sedimentation dynamics of granular flows and their comparison with additional characteristics of the benchmark experiment (Roche et al. 2010; Roche 2012), thus allowing to explore aspects of granular flows that were not addressed by Breard et al. (2019a). In contrast, the model of Breard et al. (2019a) is able to describe slight compaction and dilation processes, which is not possible in our formulation.

Numerical results reproduce reasonably well the collapse and propagation dynamics described in the analogue experiment in terms of run-out distance and pore pressure, and they allow to constrain the effective diffusion coefficient that characterizes the granular material considered.

However, even though the model captures the general shape of the resulting deposits, the thickness tends to be under-estimated in proximal domains and over-estimated in distal domains. Potential sources of systematic differences between analogue experiments and our numerical model are the dynamics of gate opening and simplifications in the mathematical description such as the non-compressibility of the granular flow and the assumption of a constant effective diffusion coefficient in space and time.

Interestingly, our estimates of the effective diffusion coefficient are consistent with experimental measurements on static defluidizing beds (Roche et al. 2010) and are one order of magnitude smaller than the theoretical value, which fails completely in predicting the behaviour of the studied analogue experiment (see Fig. 1d). The discrepancy between the theoretical value and experiment-derived estimates (Roche et al. 2010; Montserrat et al. 2012) is a major unsolved issue related to pore pressure diffusion in granular materials. Breard et al. (2019b) showed that if the volume of air in a windbox at the base of an experimental granular column is significant compared to the volume of air in the column, then the measured diffusion coefficient is larger than predicted theoretically. However, we made recently further pore pressure diffusion tests in a device with a windbox whose volume was less than ~0.05 % of the volume of air in the granular column, and we found a positive correlation between the diffusion coefficient and the column height (in preparation). Therefore, though a windbox affects the estimates of pore pressure diffusion coefficient, it cannot be invoked to explain differences of more than one order of magnitude between experimental and theoretical estimates, and thus additional investigation is still required to understand this discrepancy. In the case of the numerical simulations presented here, we note that the effective diffusion coefficients $\kappa = 0.015 - 0.035\ \mathrm{m}^2/\mathrm{s}$ giving the best agreement with the experimental data are those typical of static bed heights of ~15–25 cm, which are about half the height of the initial column in the dam-break configuration. This typical height seems to be the best compromise between the height of the column released and that of the resulting flow.

Despite that main differences in flow dynamics due to different diffusion coefficients arise during only the first ~17-22% of the total propagation time, they can cause significant changes in the resulting run-out distance. In contrast, during the later phases of flow propagation, once pore pressure has diffused significantly, the non-fluidized conditions of the flow produce a similar stopping dynamics in all the simulations studied. These results suggest that understanding the processes controlling the generation and evolution of pore pressure (e.g. internal gas-particle motion, air ingestion, particle settling and diffusion; Sweeney and Valentine 2017; Valentine and Sweeney 2018; Valentine 2020; Fries et al. 2021) at early propagation stages can be particularly critical in controlling the whole granular flow, regardless of possible mechanisms able to generate pore pressure during later propagation stages (Benage et al. 2016; Breard et al. 2018; Chédeville and Roche 2015, 2018; Lube et al. 2019), which are not taken into account in our numerical model and are expected to be negligible in the benchmark experiment. In simulations on horizontal surfaces with effective diffusion coefficients compatible with the benchmark experiment, we observe an increase of run-out distance by a factor of ~1.8–2.2 when compared with dry granular flows. Thus, fluidization processes represent a critical factor in the evaluation of PDC hazard.

Additionally, this work provides insights for understanding some aspects of the dynamics of fluidized granular flows such as the evolution of pore pressure in time and space, the deposition process, and the effect of inclined topographies. These aspects are discussed below:

a) Our simulations of initially fluidized flows present an initial phase dominated by pore pressure advection and a later phase controlled by pore pressure diffusion up to reach stationary conditions. The transition between these phases is influenced by the effect of front velocity on flow stretching because pore pressure diffuses faster in thinner flows.

Importantly, these results suggest that the fluidization effect in increasing the maximum run-out distance may be self-limited, particularly on steep slopes. In fact, high pore pressure reduces friction and causes faster granular flows able to travel larger distances, but in turn fast propagation causes reduction in flow thickness, which causes faster pore pressure diffusion.

b) The basal pore pressure simulated at a given point along the channel shows an over-pressure phase coincident with the passage of the flow head, while the pressure signal measured in experiments beneath the flow substrate interface, which represents the difference between the pressure at the flow base and the ambient atmospheric pressure, is characterized by a short under-pressure phase followed by a longer over-pressure stage. Although comparing these data is not straightforward because the experimental data are partially influenced by processes not considered in our model, in this work we analyzed the main characteristics of these signals and we also considered the influence of the basal slip conditions, as suggested in the literature (Roche et al. 2010; Breard et al. 2019a). We show that the relationship between distance along the channel and the maximum pressure reached during the flow passage is remarkably similar in simulations and experiments, which indicates that our model is able to capture reasonably well the evolution of pore pressure within the granular flow. This suggests that the effect of compaction and dilatancy processes (Bouchut et al. 2016, 2021) is limited once the flow front has passed, and that the pore pressure effect in the propagation of granular flows can be modeled considering only advection. Moreover, we show that the magnitude of the under-pressure phase measured in experiments can be successfully quantified by considering the slip velocity at the channel base, as proposed by Breard et al. (2019a).

c) Our simulations suggest that deposition is close to the *en masse* end-member. In fact, for a given point along the channel, the time-span during which deposition occurs is much smaller than the timescale of granular flow propagation. Our results show that the position at which the maximum of sedimentation rate occurs advances monotonically from the reservoir and it is strongly influenced by the surface slope angle, while the effect of the pore pressure diffusion coefficient is small. Our conclusion on deposition is relevant for the experimental configuration considered but it is not necessarily applicable for natural systems of significantly larger scale. In nature, in fact, progressive aggradation can operate if onset of deposition occurs at early stages, the flow thickness is large and the deposition rate is low (see Fig. 12 of Roche 2012).

d) Numerical simulations on inclined surfaces have shown that a low slope angle (up to 10°) is able to increase the run-out distance by a factor of 2.05 – 2.25 when compared with horizontal surfaces. This has major implications for pyroclastic density currents, which typically propagate at gentle slope angles. A remarkable example where the regional slope could exert a significant effect is the Cerro Galan Ignimbrite (NW Argentina; Francis et al. 1983; Cas et al. 2011; Lesti et al. 2011), which presents a maximum run-out distance of ~70 km and was emplaced on a regional regular slope of a few degrees. Cas et al. (2011) also suggested an important effect of gas pore pressure in the reduction of friction between the flow and the substrate in this case study. Another example is the Peach Spring Tuff (USA), formed by PDCs that travelled >170 km from the eruptive centre and propagated on substrates with gentle slope angles (Valentine et al. 1989; Roche et al. 2016). In this case as well, a significant influence of gas pore pressure in the resulting run-out distance has been suggested (Roche et al. 2016). Notice that though regional slope may enhance the runout distance of PDCs, recent advances suggest that the latter is controlled fundamentally by the discharge rate (Roche et al. 2021).

5. Concluding remarks

The numerical simulations presented in this work and their comparison with published experimental data have revealed that:

(1) Even though the pore pressure diffusion coefficient probably varies in space and time in dam-break fluidized granular flows, a constant (effective) pore pressure diffusion coefficient can be estimated to capture reasonably well the flow dynamics in terms of run-out distance, temporal evolution of pore fluid pressure, and shape of the deposit.

(2) Pore pressure increases significantly the run-out distance of initially fluidized granular flows when compared with dry granular flows (e.g., by a factor of ~1.8 – ~2.2 on horizontal slopes). Therefore, taking into account pore fluid pressure appears critical for modelling dense PDCs in the context of volcanic hazard assessment.

(3) A significant effect in granular flow run-out is also exerted by the substrate slope angle. For given fluidization conditions, an increase of slope angle from 0° to 10° produces an increment of the run-out distance of 105 – 125%.

(4) The effect of fluidization in increasing run-out distance may be self-limited because the higher velocity due to fluidization tends to reduce flow thickness, which induces faster pore pressure diffusion.

(5) The pore pressure evolution in initially fluidized granular flows is mainly controlled by the diffusion coefficient, while the effect of the angle slope of the substrate is limited.

(6) In the dam-break configuration at laboratory scale, the onset of the deposition of granular flows occurs with a significant delay with respect to the front propagation. Once deposition starts, the position at which the maximum sedimentation rate occurs advances monotonically with time at a velocity significantly larger than the flow front velocity. The dynamics of sedimentation in the studied experimental configuration, which is a direct consequence of the rheological model adopted and does not require

calibrated inputs to set the sedimentation rate, is close to the *en masse* end-member model, but more progressive aggradation may operate in nature.

(7) Our model describes depth-dependent variations of the properties of granular flows considering high-aspect ratio dam-break configurations. Moreover, the possibility of exploring granular flows at larger length-scale makes this model a promising tool for investigating the factors controlling the dynamics of long run-out PDCs in nature.

Acknowledgement

This research was financed by the French government IDEX-ISITE initiative 16-IDEX-0001 (CAP 20-25). This is Laboratory of Excellence ClerVolc contribution number 501. The numerical simulations have been performed on a DELL cluster with 32 processors Xeon E2650v2 (8 cores), 1 To of total memory and an infiniband (FDR 56Gb/s) connecting network. This cluster has been financed by the French Government Laboratory of Excellence initiative n°ANR-10-LABX-0006. We thank an anonymous referee, Dr. Gert Lube and Dr. Greg Valentine for their useful comments and suggestions to improve this work.

References

Balay S, Abhyankar S, Adams M, Brown J, Brune P, Buschelman K, Dalcin L, Dener A, Eijkhout V, Gropp W, Karpeyev D, Kaushik D, Knepley M, May D, McInnes LC, Mills R, Munson T, Rupp K, Sanan P, Smith B, Zampini S, Zhang H (2018a) PETSc Users Manual Revision 3.10 (Technical Report ANL-95/11 - Revision 3.10). Argonne National Laboratory (ANL), Argonne, IL (United States).

Balay S, Abhyankar S, Adams M, Brown J, Brune P, Buschelman K, Dalcin L, Dener A, Eijkhout V, Gropp W, Kaushik D, Knepley M, May D, McInnes LC, Mills R, Munson

T, Rupp K, Sanan P, Smith B, Zampini S, Zhang H (2018b) PETSc Web page. http://www.mcs.anl.gov/petsc

Benage M, Dufek J, Mothes P (2016) Quantifying entrainment in pyroclastic density currents from the Tungurahua eruption, Ecuador: Integrating field proxies with numerical simulations. Geophysical Research Letters 43(13):6932-6941. https://doi.org/10.1002/2016GL069527

Bernard J, Kelfoun K, Le Pennec J, Vallejo Vargas S (2014) Pyroclastic flow erosion and bulking processes: comparing field-based vs modeling results at Tungurahua volcano, Ecuador. Bulletin of Volcanology 76(9):1-16. https://doi.org/10.1007/s00445-014-0858-y

Bouchut F, Fernández-Nieto E, Mangeney A, Narbona-Reina G (2016) A two-phase two-layer model for fluidized granular flows with dilatancy effects. Journal of Fluid Mechanics 801:166-221. https://doi.org/10.1017/jfm.2016.417

Bouchut F, Fernández-Nieto E, Mangeney A, Narbona-Reina G (2021) Dilatancy in dry granular flows with a compressible μ(I) rheology. Journal of Computational Physics 429:110013. https://doi.org/10.1016/j.jcp.2020.110013

Brand B, Mackaman-Lofland C, Pollock N, Bendaña S, Dawson B, Wichgers P (2014) Dynamics of pyroclastic density currents: Conditions that promote substrate erosion and self-channelization—Mount St Helens, Washington (USA). Journal of Volcanology and Geothermal Research 276:189-214. https://doi.org/10.1016/j.jvolgeores.2014.01.007

Branney M, Kokelaar P (2002) Pyroclastic density currents and the sedimentation of ignimbrites. Geological Society of London.

Breard EC, Lube G, Jones JR, Dufek J, Cronin SJ, Valentine GA, Moebis A (2016) Coupling of turbulent and non-turbulent flow regimes within pyroclastic density currents. Nature Geoscience 9(10):767-771. https://doi.org/10.1038/ngeo2794

Breard E, Dufek J, Lube G (2018) Enhanced mobility in concentrated pyroclastic density currents: An examination of a self-fluidization mechanism. Geophysical Research Letters, 45(2), 654-664. https://doi.org/10.1002/2017GL075759

Breard EC, Dufek J, Roche O (2019a) Continuum modeling of pressure-balanced and fluidized granular flows in 2-D: Comparison with glass bead experiments and implications for concentrated pyroclastic density currents. Journal of Geophysical Research: Solid Earth 124(6):5557-5583. https://doi.org/10.1029/2018JB016874

Breard EC, Jones, JR, Fullard L, Lube G, Davies C, Dufek J (2019b) The permeability of volcanic mixtures—implications for pyroclastic currents. Journal of Geophysical Research: Solid Earth 124(2):1343-1360. https://doi.org/10.1029/2018JB016544

Burgisser A (2012) A semi-empirical method to calculate the permeability of homogeneously fluidized pyroclastic material. Journal of Volcanology and Geothermal Research 243: 97-106. https://doi.org/10.1016/j.jvolgeores.2012.08.015

Burgisser A, Bergantz G (2002) Reconciling pyroclastic flow and surge: the multiphase physics of pyroclastic density currents. Earth and Planetary Science Letters 202(2):405-418. https://doi.org/10.1016/S0012-821X(02)00789-6

Bursik MI, Woods AW (1996) The dynamics and thermodynamics of large ash-flows. Bulletin of Volcanology 58:175-93. https://doi.org/10.1007/s004450050134

Cas R, Wright H, Folkes C, Lesti C, Porreca M, Giordano G, Viramonte J (2011) The flow dynamics of an extremely large volume pyroclastic flow, the 2.08-Ma Cerro Galán Ignimbrite, NW Argentina, and comparison with other flow types. Bulletin of Volcanology 73(10):1583-1609. https://doi.org/10.1007/s00445-011-0564-y

Chalayer R, Chupin L, Dubois T (2018) A bi-projection method for incompressible bingham flows with variable density, viscosity, and yield stress. SIAM Journal on Numerical Analysis 56(4):2461-2483. https://doi.org/10.1137/17M113993X

Chédeville C, Roche O (2015) Influence of slope angle on pore pressure generation and kinematics of pyroclastic flows: insights from laboratory experiments. Bulletin of Volcanology 77(11):1-13. https://doi.org/10.1007/s00445-015-0981-4

Chédeville C, Roche O (2018) Autofluidization of collapsing bed of fine particles: implications for the emplacement of pyroclastic flows. Journal of Volcanology and Geothermal Research 368:91-99. https://doi.org/10.1016/j.jvolgeores.2018.11.007

Chupin L, Dubois T (2016) A bi-projection method for Bingham type flows. Computers & Mathematics with Applications 72(5):1263-1286. https://doi.org/10.1016/j.camwa.2016.06.026

Chupin L, Dubois T, Phan M, Roche O (2021) Pressure-dependent threshold in a granular flow: Numerical modeling and experimental validation. Journal of Non-Newtonian Fluid Mechanics 291:104529. https://doi.org/10.1016/j.jnnfm.2021.104529

Cole P, Neri A, Baxter P (2015) Hazards from pyroclastic density currents. In: The Encyclopedia of Volcanoes (pp. 943-956). Academic Press.

Druitt T (1998) Pyroclastic density currents. Geological Society, London, Special Publications 145(1):145-182.

Druitt T, Avard G, Bruni G, Lettieri P, Maez F (2007) Gas retention in fine-grained pyroclastic flow materials at high temperatures. Bulletin of Volcanology 69(8):881-901. https://doi.org/10.1007/s00445-007-0116-7

Dufek J (2016) The fluid mechanics of pyroclastic density currents. Annual Review of Fluid Mechanics 48:459-485. https://doi.org/10.1146/annurev-fluid-122414-034252

Dufek J, Esposti Ongaro T, Roche O (2015) Pyroclastic density currents: processes and models. In: The Encyclopedia of Volcanoes (pp. 617-629). Academic Press.

Esposti Ongaro T, Cerminara M, Charbonnier S, Lube G, Valentine G (2020) A framework for validation and benchmarking of pyroclastic current models. Bulletin of Volcanology 82:1-17. https://doi.org/10.1007/s00445-020-01388-2

Farin M, Mangeney A, Roche O (2014) Fundamental changes of granular flow dynamics, deposition, and erosion processes at high slope angles: insights from laboratory experiments. Journal of Geophysical Research: Earth Surface 119(3):504-532. https://doi.org/10.1002/2013JF002750

Francis P, O'Callaghan L, Kretzschmar G, Thorpe R, Sparks R, Page R, De Barrio R, Gillou G, Gonzalez O (1983) The Cerro Galan ignimbrite. Nature 301(5895):51-53. https://doi.org/10.1038/301051a0

Fries A, Roche O, Carazzo G (2021) Granular mixture deflation and generation of pore fluid pressure at the impact zone of a pyroclastic fountain: Experimental insights. Journal of Volcanology and Geothermal Research 414:107226. https://doi.org/10.1016/j.jvolgeores.2021.107226

Fullmer WD, Hrenya CM (2017) The clustering instability in rapid granular and gas-solid flows. Annual Review of Fluid Mechanics 49:485-510. https://doi.org/10.1146/annurev-fluid-010816-060028

Garres-Díaz J, Bouchut F, Fernández-Nieto E, Mangeney A, Narbona-Reina G (2020) Multilayer models for shallow two-phase debris flows with dilatancy effects. Journal of Computational Physics 419:109699. https://doi.org/10.1016/j.jcp.2020.109699

Gase A, Brand B, Bradford J (2017) Evidence of erosional self-channelization of pyroclastic density currents revealed by ground-penetrating radar imaging at Mount St. Helens, Washington (USA). Geophysical Research Letters 44(5):2220-2228. https://doi.org/10.1002/2016GL072178

Giordano G, Cas RAF (2021) Classification of ignimbrites and their eruptions. Earth-Science Reviews 220:103697. https://doi.org/10.1016/j.earscirev.2021.103697

Goren L, Aharonov E, Sparks D, Toussaint R (2010) Pore pressure evolution in deforming granular material: A general formulation and the infinitely stiff approximation. Journal of Geophysical Research: Solid Earth 115(B9). https://doi.org/10.1029/2009JB007191

Gray J, Edwards A (2014) A depth-averaged μ(I)-rheology for shallow granular free-surface flows. Journal of Fluid Mechanics 755:503-534. https://doi.org/10.1017/jfm.2014.450

Gueugneau V, Kelfoun K, Roche O, Chupin L (2017) Effects of pore pressure in pyroclastic flows: numerical simulation and experimental validation. Geophysical Research Letters 44(5):2194-2202. https://doi.org/10.1002/2017GL072591

Ionescu I, Mangeney A, Bouchut F, Roche O (2015) Viscoplastic modeling of granular column collapse with pressure-dependent rheology. Journal of Non-Newtonian Fluid Mechanics 219:1-18. https://doi.org/10.1016/j.jnnfm.2015.02.006

Iverson R (1997) The physics of debris flows. Reviews of Geophysics 35(3):245-296. https://doi.org/10.1029/97RG00426

Iverson R, Denlinger R (2001) Flow of variably fluidized granular masses across three-dimensional terrain: 1. Coulomb mixture theory. Journal of Geophysical Research: Solid Earth 106(B1):537-552. https://doi.org/10.1029/2000JB900329

Jop P, Forterre Y, Pouliquen O (2006) A constitutive law for dense granular flows. Nature 441(7094):727-730. https://doi.org/10.1038/nature04801

Kelfoun K (2011) Suitability of simple rheological laws for the numerical simulation of dense pyroclastic flows and long-runout volcanic avalanches. Journal of Geophysical Research: Solid Earth 116(B8). https://doi.org/10.1029/2010JB007622

Lesti C, Porreca M, Giordano G, Mattei M, Cas R, Wright H, Folkes C, Viramonte J (2011) High-temperature emplacement of the Cerro Galán and Toconquis Group ignimbrites

(Puna plateau, NW Argentina) determined by TRM analyses. Bulletin of Volcanology 73(10):1535-1565. https://doi.org/10.1007/s00445-011-0536-2

Lube G, Breard EC, Jones J, Fullard L, Dufek J, Cronin SJ, Wang T (2019) Generation of air lubrication within pyroclastic density currents. Nature Geoscience 12(5):381-386. https://doi.org/10.1038/s41561-019-0338-2

Lube G, Breard EC, Esposti Ongaro T, Dufek J, Brand B (2020) Multiphase flow behaviour and hazard prediction of pyroclastic density currents. Nature Reviews Earth & Environment 1(7):348-365. https://doi.org/10.1038/s43017-020-0064-8

Marino B, Thomas L, Linden P (2005) The front condition for gravity currents. Journal of Fluid Mechanics 536:49-78. https://doi.org/10.1017/S0022112005004933

Montserrat S, Tamburrino A, Roche O, Niño Y (2012) Pore fluid pressure diffusion in defluidizing granular columns. Journal of Geophysical Research: Earth Surface 117(F2). https://doi.org/10.1029/2011JF002164

Neri A, Esposti Ongaro T, Voight B, Widiwijayanti C (2015) Pyroclastic density current hazards and risk. In: Volcanic Hazards, Risks and Disasters (pp. 109-140). Elsevier.

Osher S, Fedkiw R (2001) Level set methods: an overview and some recent results. Journal of Computational Physics 169(2):463-502. https://doi.org/10.1006/jcph.2000.6636

Roche O (2012) Depositional processes and gas pore pressure in pyroclastic flows: an experimental perspective. Bulletin of Volcanology 74(8):1807-1820. https://doi.org/10.1007/s00445-012-0639-4

Roche O, Montserrat S, Niño Y, Tamburrino A (2010) Pore fluid pressure and internal kinematics of gravitational laboratory air-particle flows: Insights into the emplacement dynamics of pyroclastic flows. Journal of Geophysical Research: Solid Earth 115(B9). https://doi.org/10.1029/2009JB007133

Roche O, Buesch D, Valentine G (2016) Slow-moving and far-travelled dense pyroclastic flows during the Peach Spring super-eruption. Nature Communications 7(1):1-8. https://doi.org/10.1038/ncomms10890

Roche O, Azzaoui N, Guillin A (2021) Discharge rate of explosive volcanic eruption controls runout distance of pyroclastic density currents. Earth and Planetary Science Letters 568:117017. https://doi.org/10.1016/j.epsl.2021.117017

Rowley P, Roche O, Druitt T, Cas R (2014) Experimental study of dense pyroclastic density currents using sustained, gas-fluidized granular flows. Bulletin of Volcanology 76(9):1-13. https://doi.org/10.1007/s00445-014-0855-1

Savage S, Iverson R (2003) Surge dynamics coupled to pore-pressure evolution in debris flows. In : Proc. 3rd Int. Conf. on Debris-Flow Hazards Mitigation: Mechanics, Prediction, and Assessment. Edited by: Rickenmann D, Chen CL. Millpress, Rotterdam (pp. 503-514).

Shimizu H, Koyaguchi T, Suzuki Y (2019) The run-out distance of large-scale pyroclastic density currents: a two-layer depth-averaged model. Journal of Volcanology and Geothermal Research 381:168-184. https://doi.org/10.1016/j.jvolgeores.2019.03.013

Smagorinsky J (1963) General circulation experiments with the primitive equations: I. The basic experiment. Monthly Weather Review 91(3):99-164.

Sweeney M, Valentine G (2017) Impact zone dynamics of dilute mono-and polydisperse jets and their implications for the initial conditions of pyroclastic density currents. Physics of Fluids 29(9):093304. https://doi.org/10.1063/1.5004197

Valentine G (2019) Preface to the topical collection—pyroclastic current models: benchmarking and validation. Bulletin of Volcanology 81:69. https://doi.org/10.1007/s00445-019-1328-3

Valentine G (2020) Initiation of dilute and concentrated pyroclastic currents from collapsing mixtures and origin of their proximal deposits. Bulletin of Volcanology 82(2):1-24. https://doi.org/10.1007/s00445-020-1366-x

Valentine G, Buesch D, Fisher R (1989) Basal layered deposits of the Peach Springs Tuff, northwestern Arizona, USA. Bulletin of Volcanology 51(6):395-414. https://doi.org/10.1007/BF01078808

Valentine G, Doronzo D, Dellino P, de Tullio M (2011) Effects of volcano profile on dilute pyroclastic density currents: numerical simulations. Geology 39(10):947-950. https://doi.org/10.1130/G31936.1

Valentine G, Sweeney M (2018) Compressible flow phenomena at inception of lateral density currents fed by collapsing gas-particle mixtures. Journal of Geophysical Research: Solid Earth 123(2):1286-1302. https://doi.org/10.1002/2017JB015129

Wilson C (1984) The role of fluidization in the emplacement of pyroclastic flows, 2: experimental results and their interpretation. Journal of Volcanology and Geothermal Research 20(1-2):55-84. https://doi.org/10.1016/0377-0273(84)90066-0

Figures

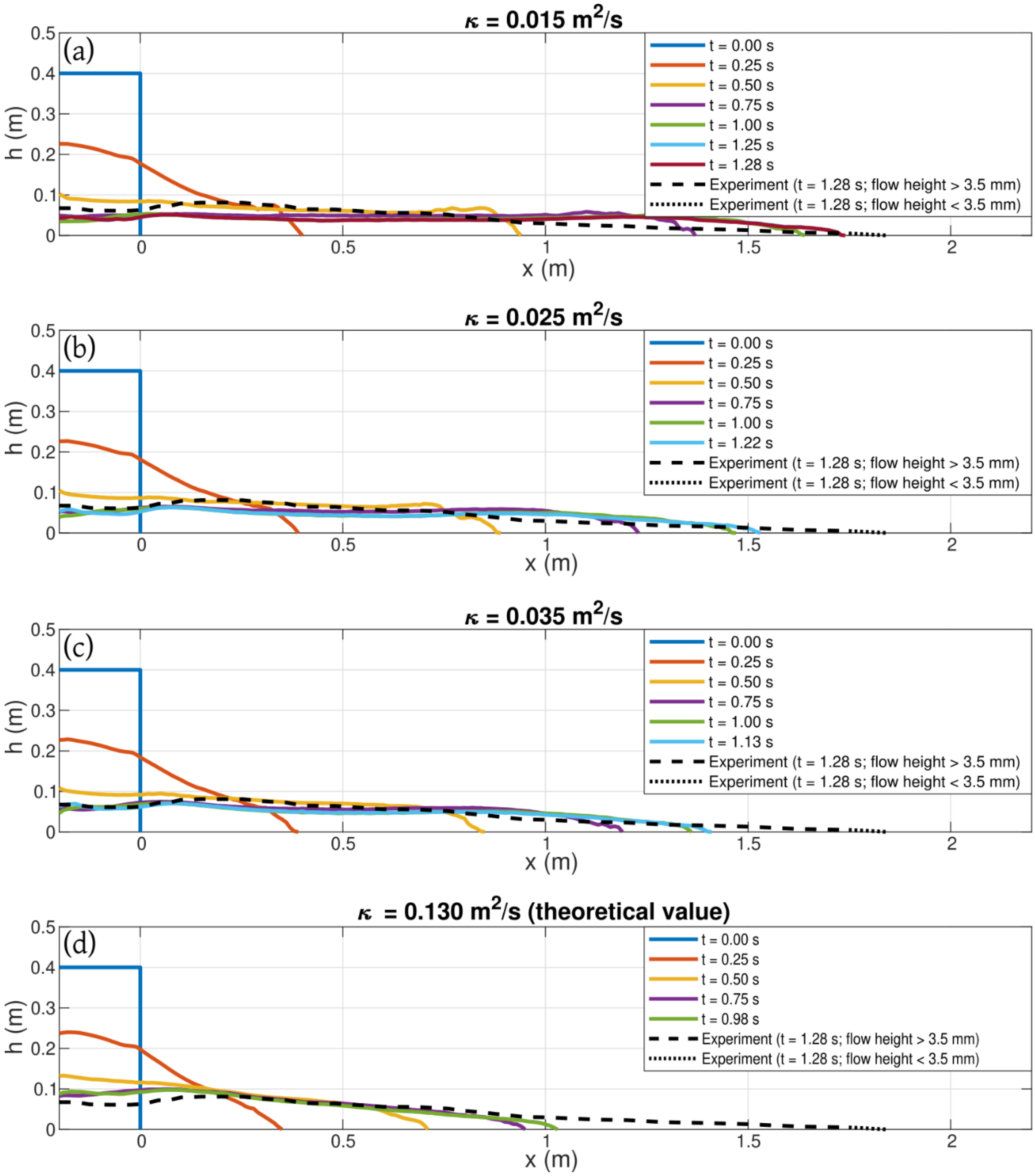

Figure 1. Surface profiles of the granular flows at different times after release (see legends) in four simulations performed on horizontal planes, considering initially fluidized conditions and different values of the effective diffusion coefficient (κ, see titles). The final surface profile of the benchmark analogue experiment is also included (Roche et al. 2010).

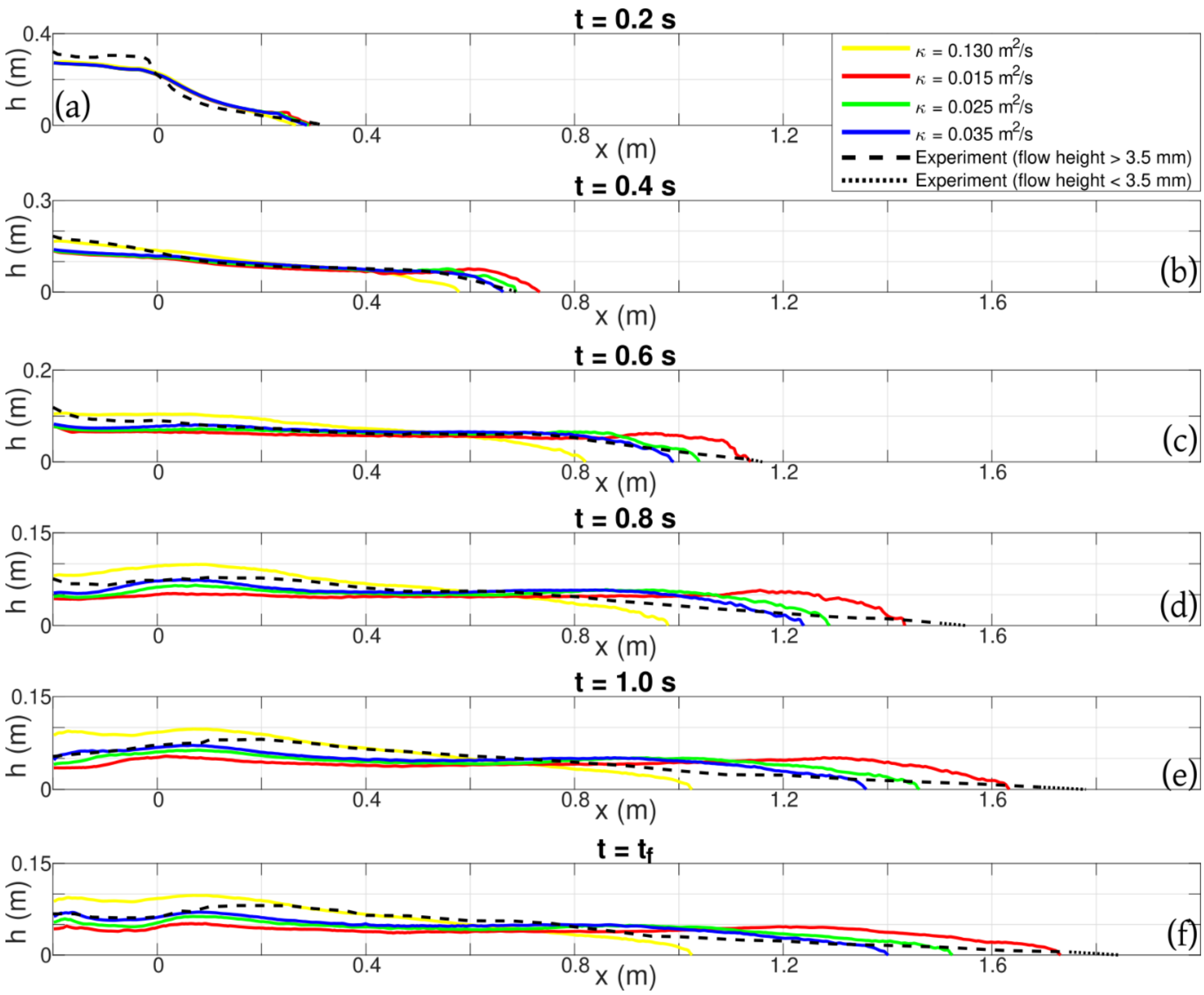

Figure 2. Surface profiles of the granular flows at different times after release in four simulations performed on horizontal planes, considering initially fluidized conditions and different values of the effective diffusion coefficient (κ, see legend). The evolution of the surface profile of the benchmark analogue experiment is also included (Roche et al. 2010).

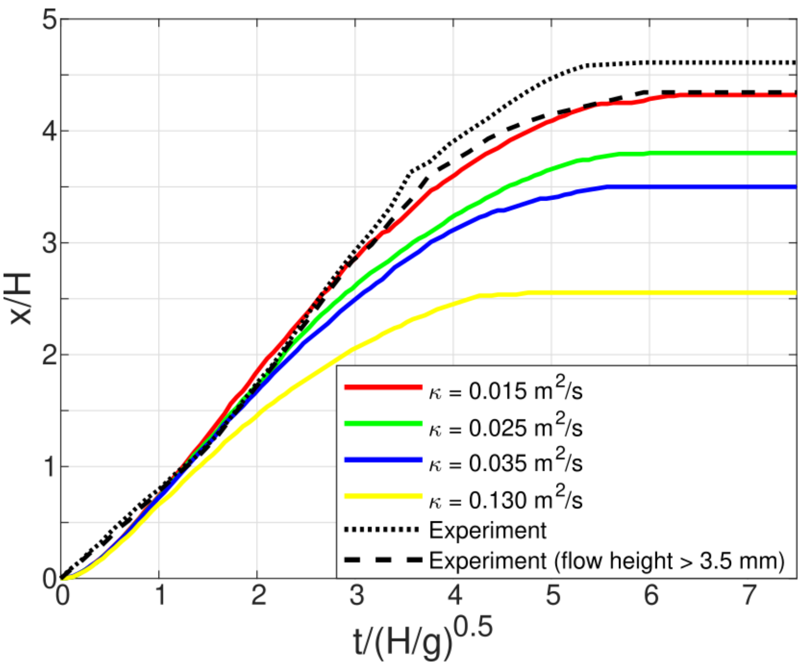

Figure 3. Temporal evolution of the front position of the granular flows in four simulations performed on horizontal planes, considering initially fluidized conditions and different values of the effective diffusion coefficient (κ, see legend). The temporal evolution of the front position of the benchmark analogue experiment is shown as well (see legend; Roche et al. 2010). Because our simulations are not able to describe flow thicknesses lower than 3.5 mm (i.e. the cell size used in numerical simulations), we also include the experimental data considering only flow thicknesses above this threshold in the definition of the front position. Both axes are normalized using ad-hoc factors in order to produce non-dimensional results ($H = 0.4$ m and $g = 9.8$ m/s^2).

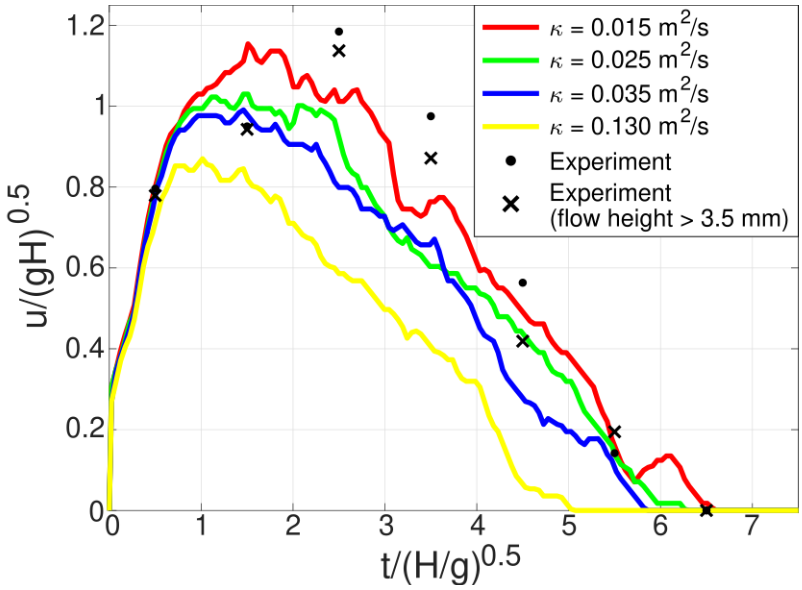

Figure 4. Temporal evolution of the front velocity of the granular flows in four simulations performed on horizontal planes, considering initially fluidized conditions and different values of the effective diffusion coefficient (κ, see legend). A moving average function was applied to these curves, considering a time window of 0.1 s. The evolution of the front velocity of the benchmark analogue experiment is shown as well (see legend; Roche et al. 2010). Because our simulations are not able to describe flow thicknesses lower than 3.5 mm (i.e. the cell size used in numerical simulations), we include the experimental data considering only flow thicknesses above this threshold in the definition of the front position. Both axes are normalized using ad-hoc factors in order to produce non-dimensional results ($H = 0.4$ m and $g = 9.8$ m/s^2). Note that the theoretical value for the maximum velocity in a dam-break experiment of an inviscid flow is $u/\sqrt{gH} = \sqrt{2} \approx 1.4$ (Marino et al. 2005).

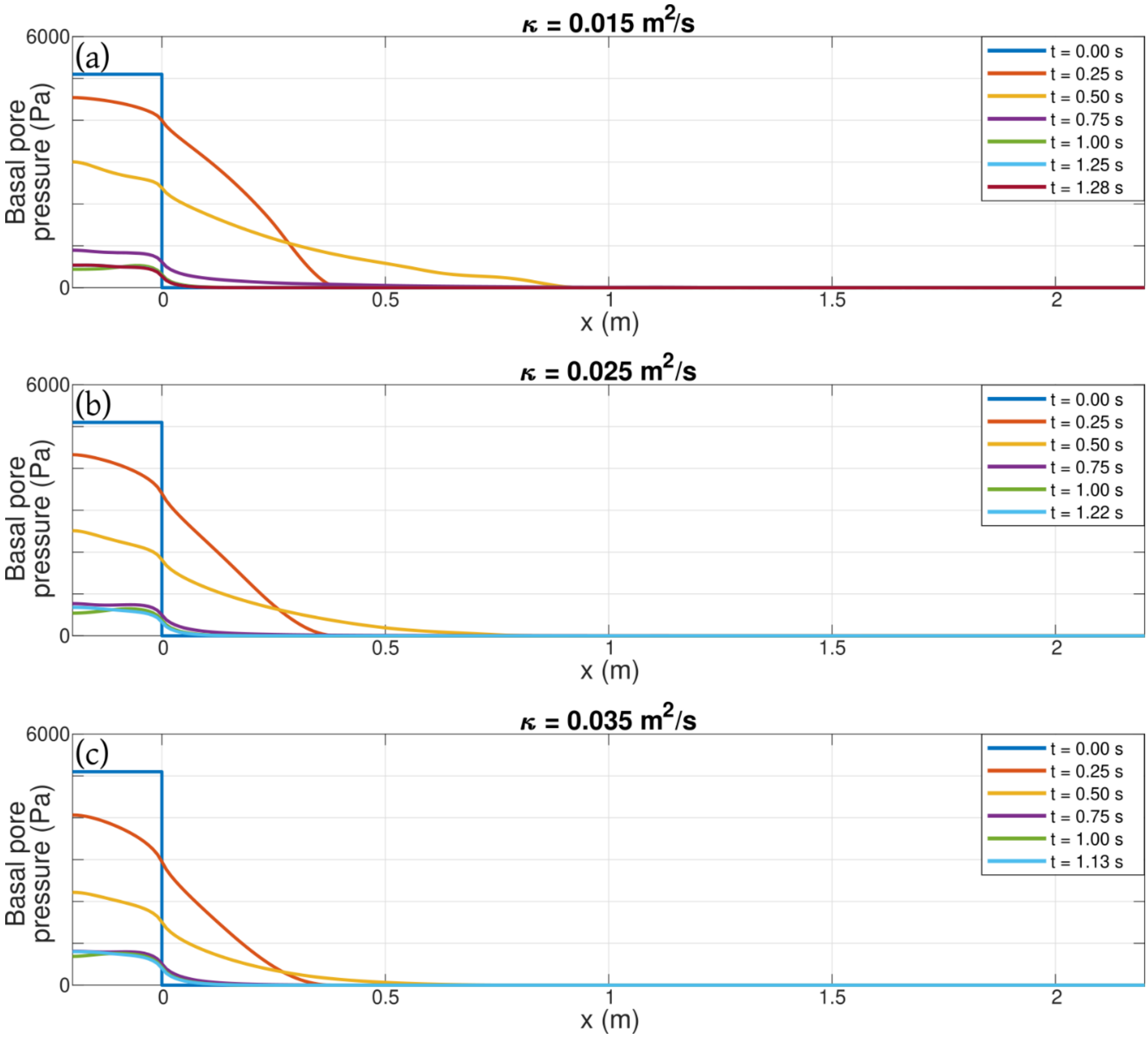

Figure 5. Basal pore pressure profiles of the granular flows at different times after release (see legends) in three simulations performed on horizontal planes, considering initially fluidized conditions and different values of the effective diffusion coefficient (κ, see titles). Note that the ratio between basal pore pressure and the lithostatic pressure ($p_f/\rho g h$), not shown here, represents the degree of fluidization (see Supplementary Figure S1). Full fluidization occurs when $p_f/\rho g h$ is larger than one.

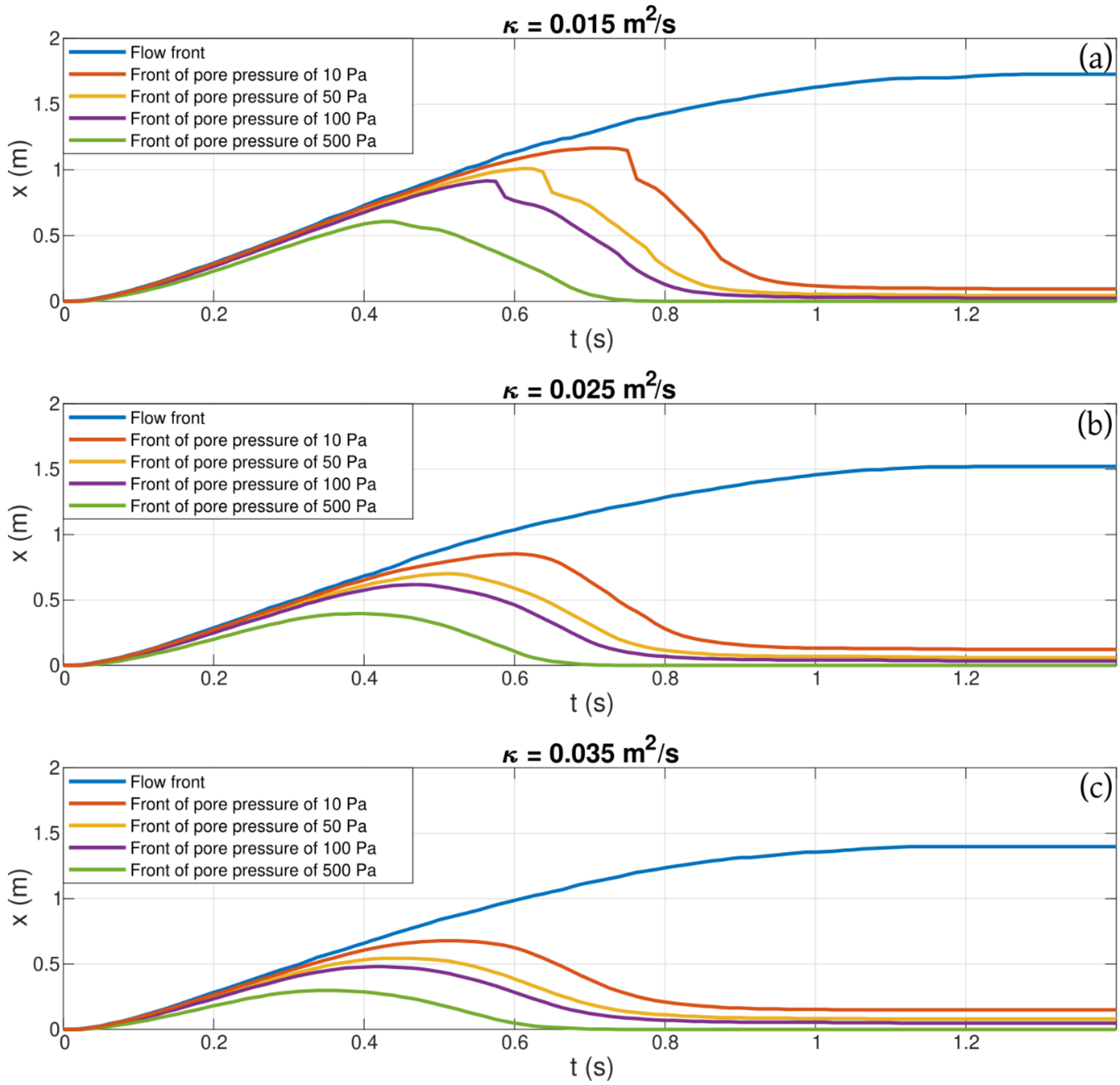

Figure 6. Temporal evolution of the front position and a set of iso-pressure fronts (i.e. the position along the x-axis at which specific values of pore pressure are reached as a function of time, see legends) in three simulations performed on horizontal planes, considering initially fluidized conditions and different values of the effective diffusion coefficient (κ, see titles).

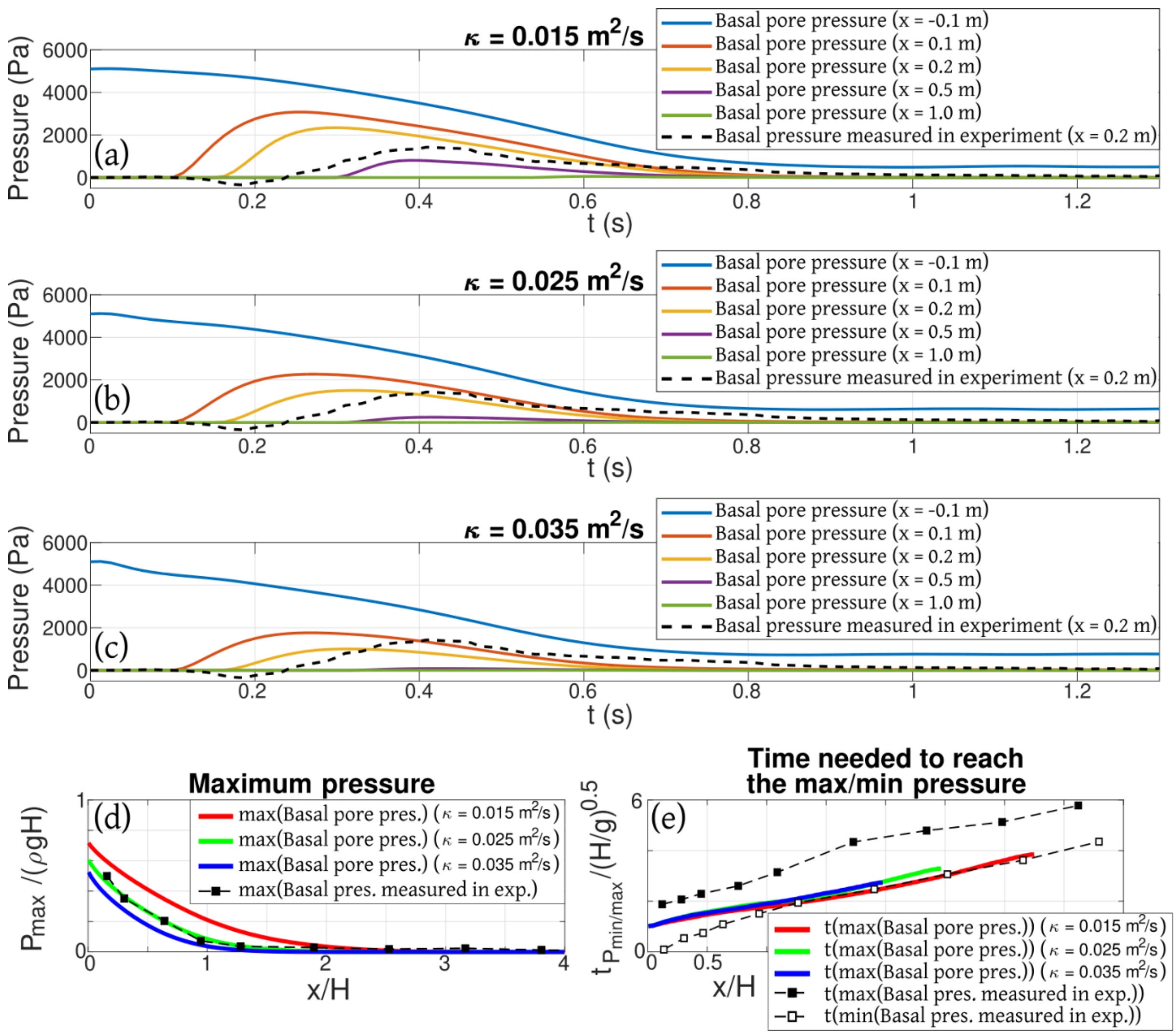

Figure 7. (a-c) Temporal evolution of basal pore pressure at different positions (see legends) in simulations on horizontal planes, considering initially fluidized conditions and different values of the effective diffusion coefficient (κ, see titles). Experimental data are also presented (Roche et al. 2010). (d) Maximum normalized values of basal pressure in numerical simulations and in the benchmark experiment as a function of horizontal distance (see legend; Roche et al. 2010). (e) Time needed to reach the extreme values of basal pressure (i.e. minimum, if present, and maximum values) at the channel base in numerical simulations and in the benchmark experiment (see legend; Roche et al. 2010).

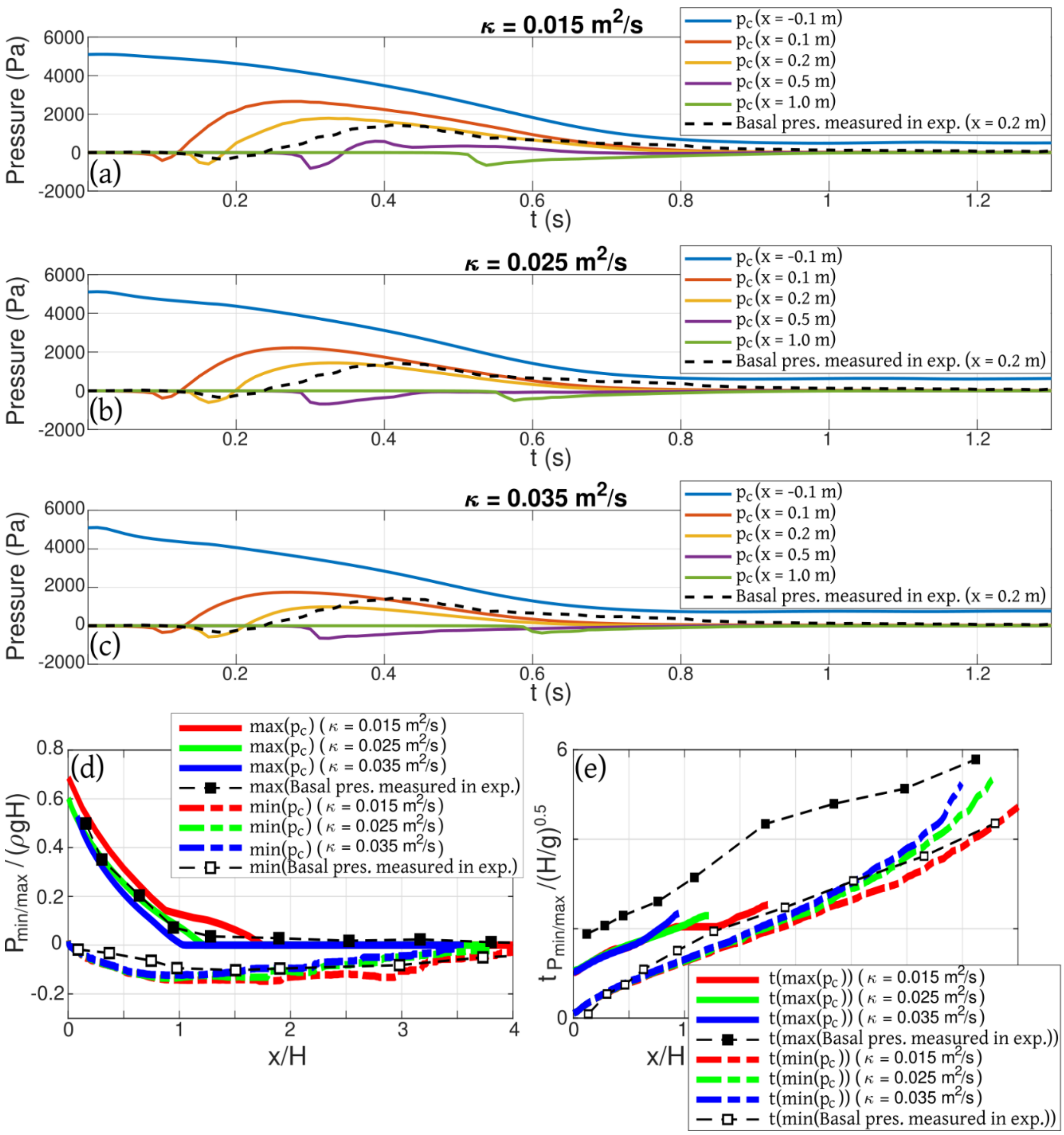

Figure 8. (a-c) Temporal evolution of p_c (see equation (11)) at different positions (see legends) in simulations performed on horizontal planes, considering initially fluidized conditions and different values of the effective diffusion coefficient (κ, see titles). Experimental data are also presented (Roche et al. 2010), which describe the difference between the pressure generated by the flow above a sensor located at $x = 0.2$ m and the ambient atmospheric pressure. (d) Maximum normalized values of p_c and differential pressure with respect to the atmosphere in numerical simulations and in the benchmark experiment, respectively, as a function of

horizontal distance (see legend; Roche et al. 2010). (e) Time needed to reach the extreme values (i.e. minimum and maximum values) of p_c and of differential pressure with respect to the atmosphere in numerical simulations and in the benchmark experiment (Roche et al. 2010), respectively (see legend).

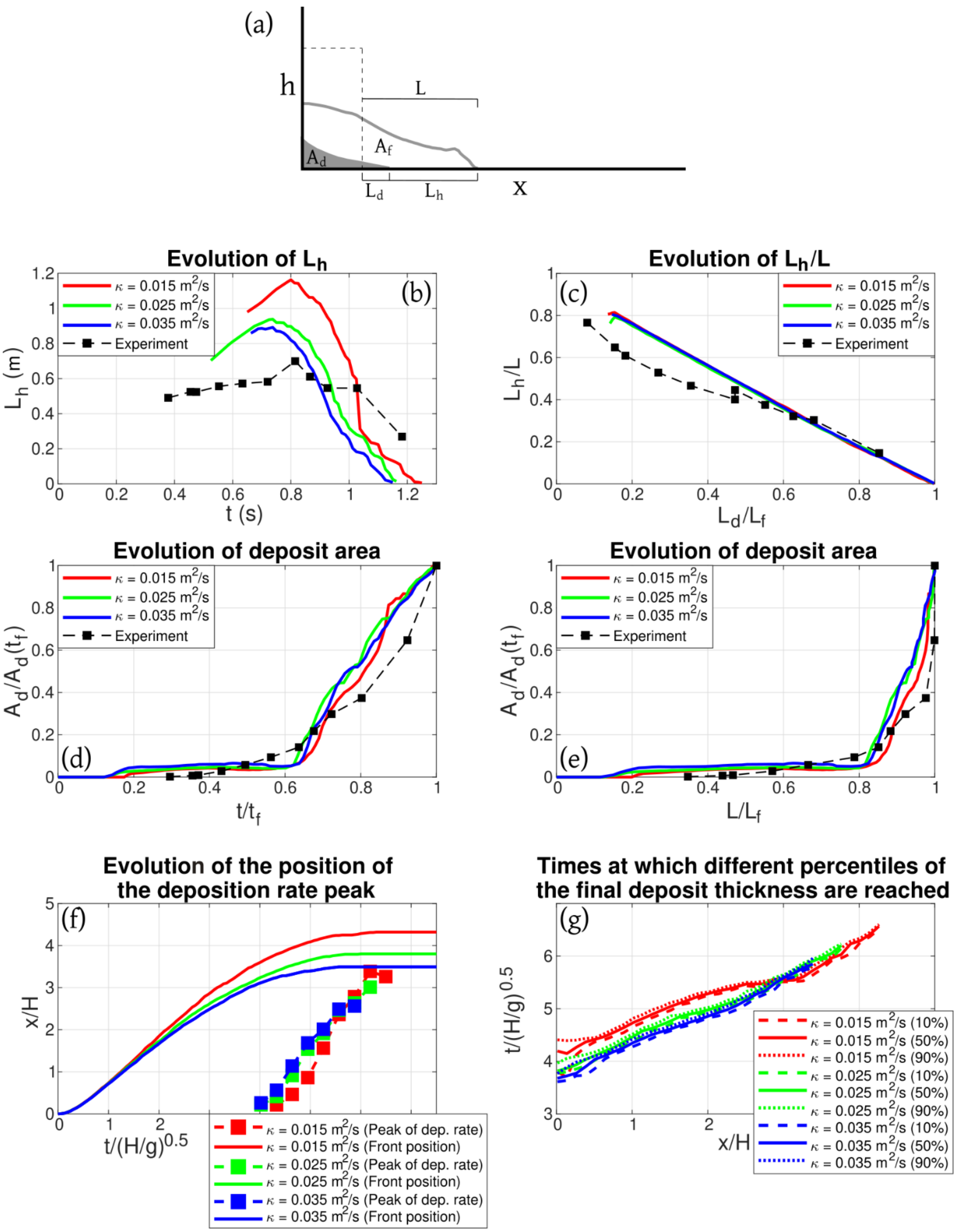

Figure 9. Plots describing the deposition dynamics of particles in our numerical simulations. (a) Schematic figure showing the definitions used to describe the deposition dynamics of the modeled granular flows. (b) Temporal evolution of the sliding head length (L_h, see panel a) in simulations performed on horizontal planes, considering initially fluidized conditions and

different values of the effective diffusion coefficient (κ, see legend). (c) L_h/L as a function of L_d/L_f (see panel a) in the same set of simulations, where $L_f = L(t_f)$ and t_f is the final time. (d) Temporal evolution of $A_d/A_d(t_f)$ (see panel a) in the same set of simulations. (e) $A_d/A_d(t_f)$ as a function of L/L_f (see panel a) in the same set of simulations. (f) Temporal evolution of the position at which the peak of deposition rate is modeled in the same set of simulations. The front position is also included. (g) Times at which different percentiles (10%, 50% and 90%) of the final deposit thickness are reached as a function of distance along the x-axis, for the same set of simulations. In panels (b)-(e) we include data from the benchmark analogue experiment (Roche 2012).

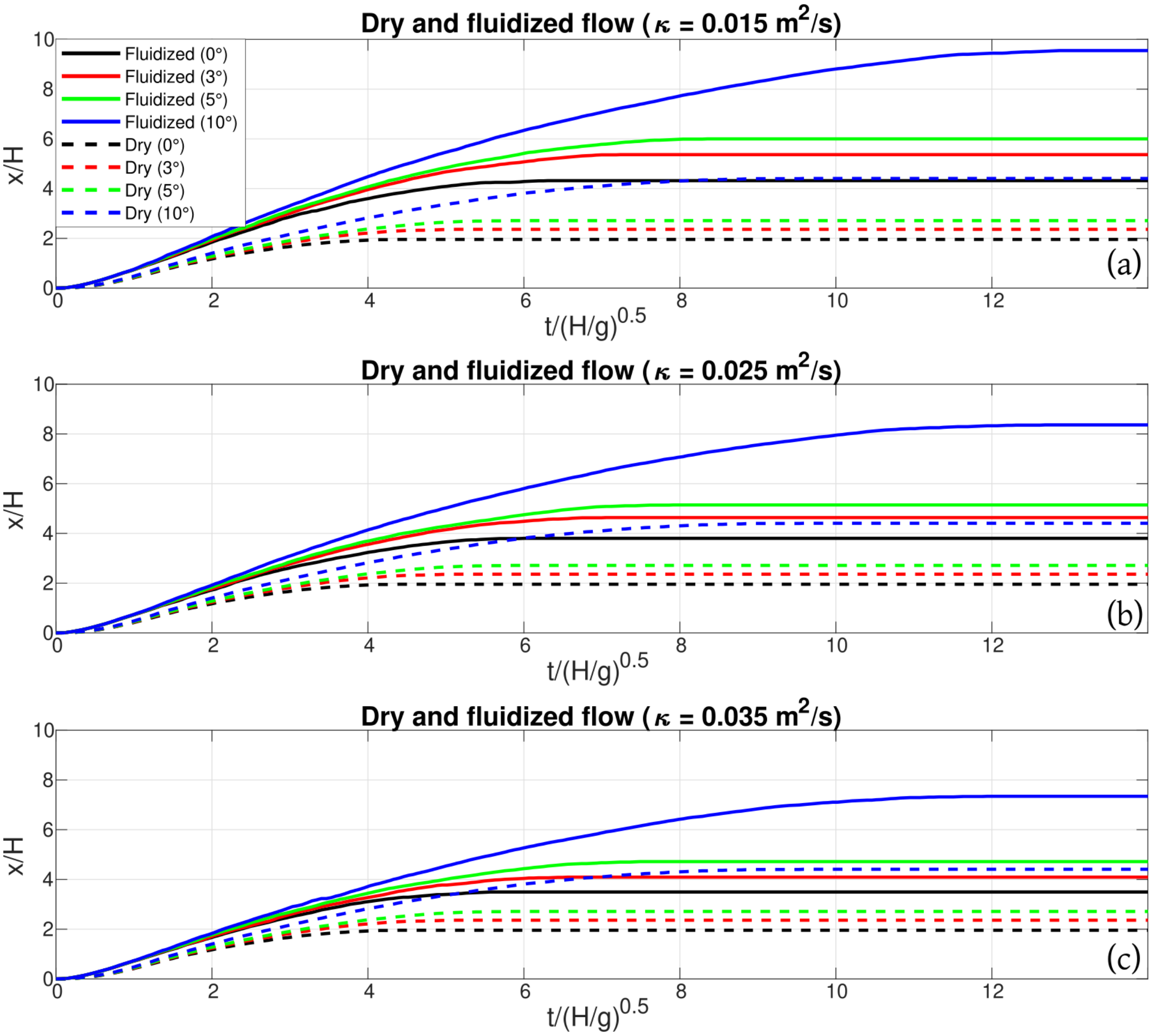

Figure 10. Temporal evolution of the front position of the granular flows in simulations with variable initial fluidization conditions (dry and fluidized flows) and different values of the effective diffusion coefficient and surface slope angle (see titles and legend).

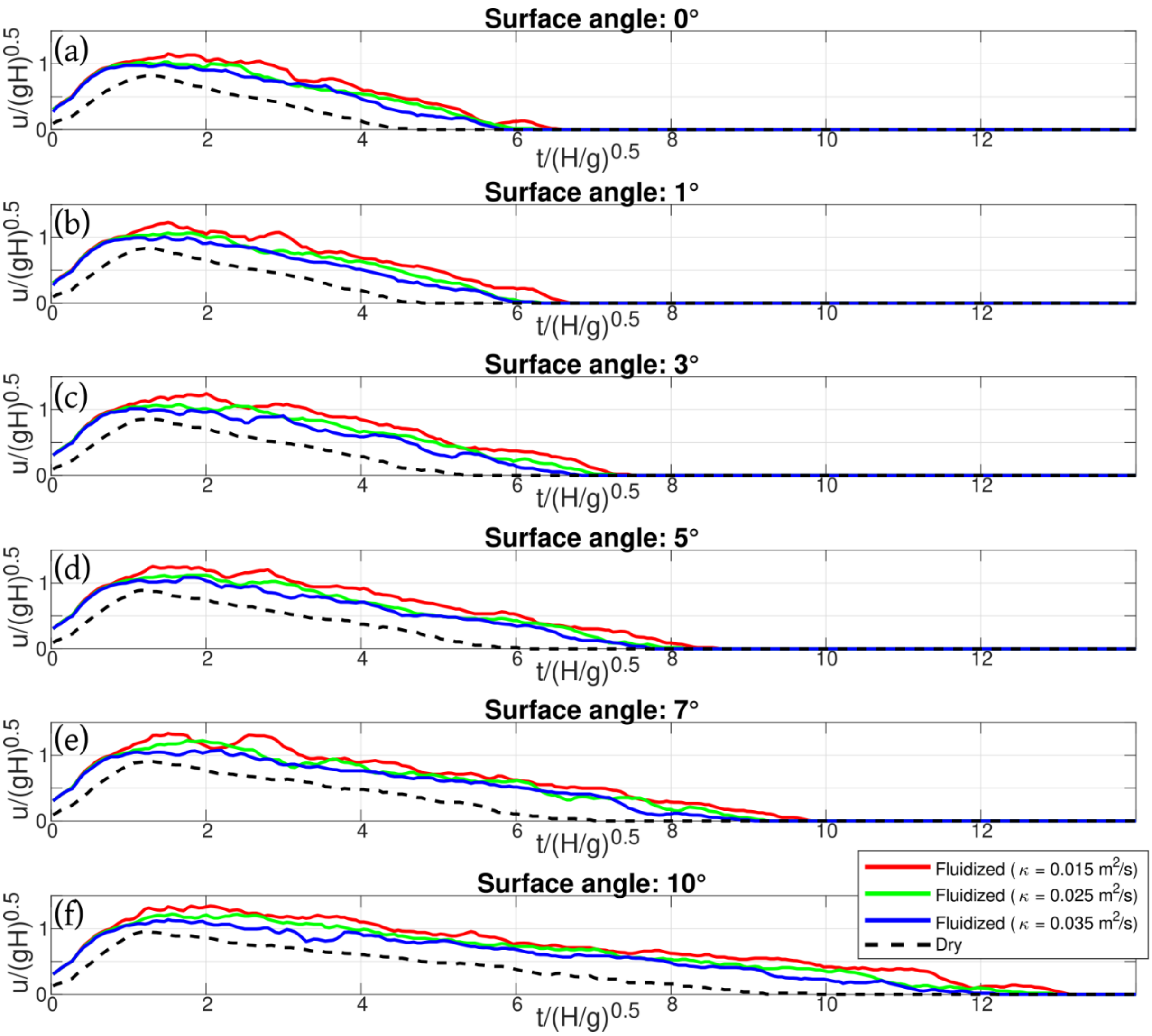

Figure 11. Temporal evolution of the front velocity of the granular flows in simulations with variable initial fluidization conditions (dry and fluidized flows) and different values of the effective diffusion coefficient and surface slope angle (see titles and legend). A moving average function was applied to these curves, considering a time window of 0.1 s.

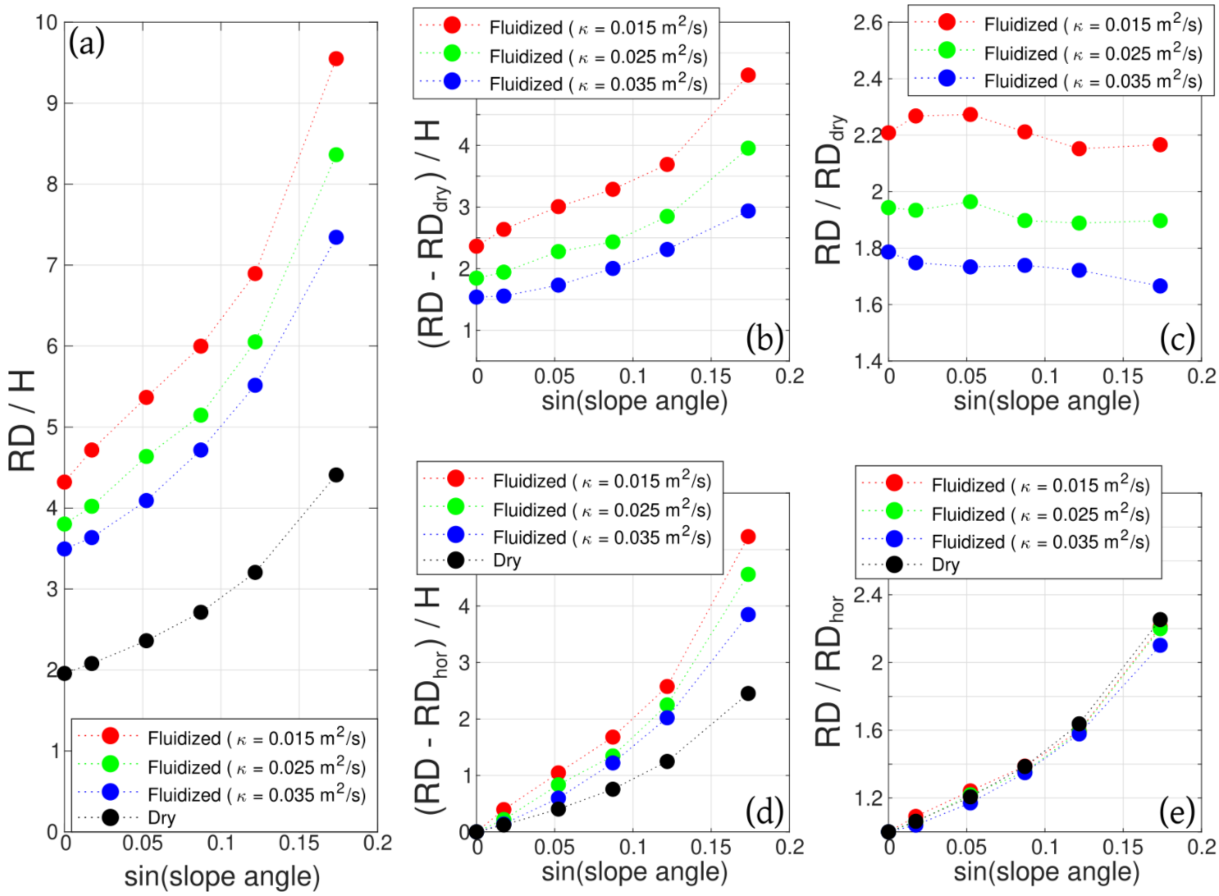

Figure 12. Comparison of the run-out distance of granular flows in simulations performed considering variable initial conditions (dry and fluidized flows) and different effective diffusion coefficients as a function of the surface slope angle. We use the function $\sin(\cdot)$ in the x-axes because it is the driving component of gravity. RD/H: run-out distance over initial column height (H). $(\mathrm{RD}-\mathrm{RD}_{\mathrm{dry}})/\mathrm{H}$: increase of run-out distance over H with respect to dry flows. $\mathrm{RD}/\mathrm{RD}_{\mathrm{dry}}$: ratio of run-out distance with respect to dry flows. $(\mathrm{RD}-\mathrm{RD}_{\mathrm{hor}})/\mathrm{H}$: increase of run-out distance over H with respect to a flow propagated over a horizontal surface. $\mathrm{RD}/\mathrm{RD}_{\mathrm{hor}}$: ratio of run-out distance with respect to a flow propagated over a horizontal surface.

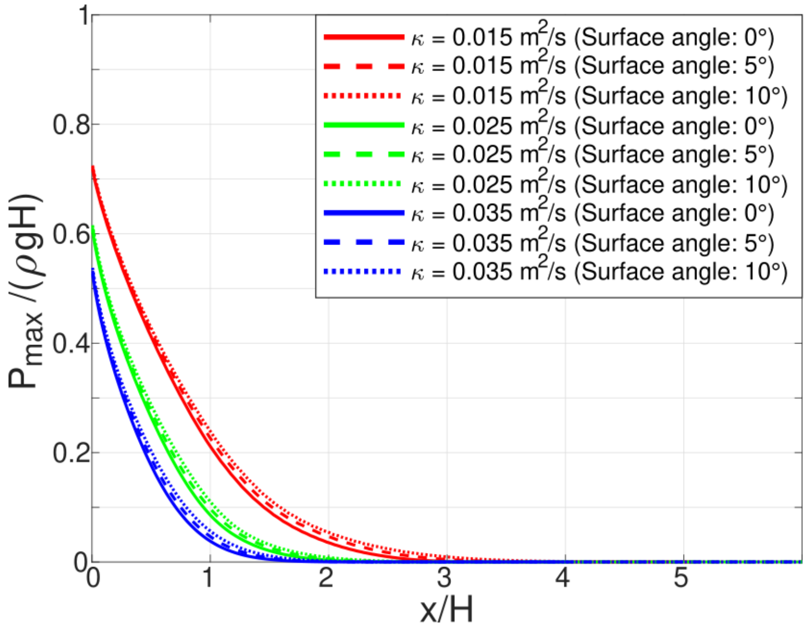

Figure 13. Maximum normalized basal pore pressure during the propagation of fluidized granular flows as a function of horizontal distance in numerical simulations with different effective diffusion coefficients and surface slope angles (see legend).

917

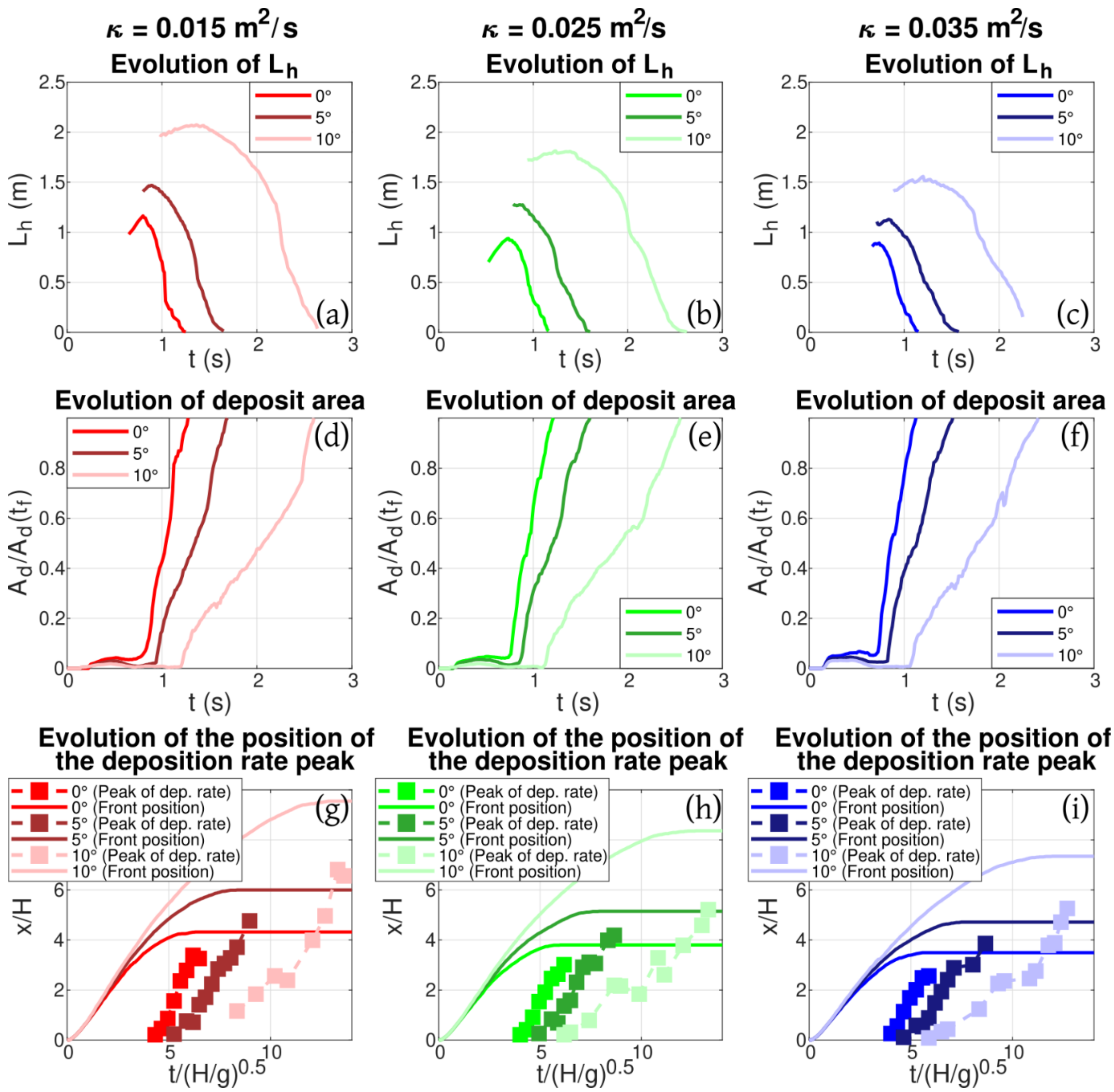

918 **Figure 14.** (a-c) Temporal evolution of L_h (see Figure 9a) in simulations performed on
919 horizontal and inclined planes (see legends), considering initially fluidized conditions and
920 different values of the effective diffusion coefficient (κ, see titles). (d-f) Temporal evolution of
921 $A_d/A_d(t_f)$ (see Figure 9a) in the same set of simulations. (g-i) Temporal evolution of the
922 position at which the peak of deposition rate is modeled in the same set of simulations. The
923 front position is also included.

924